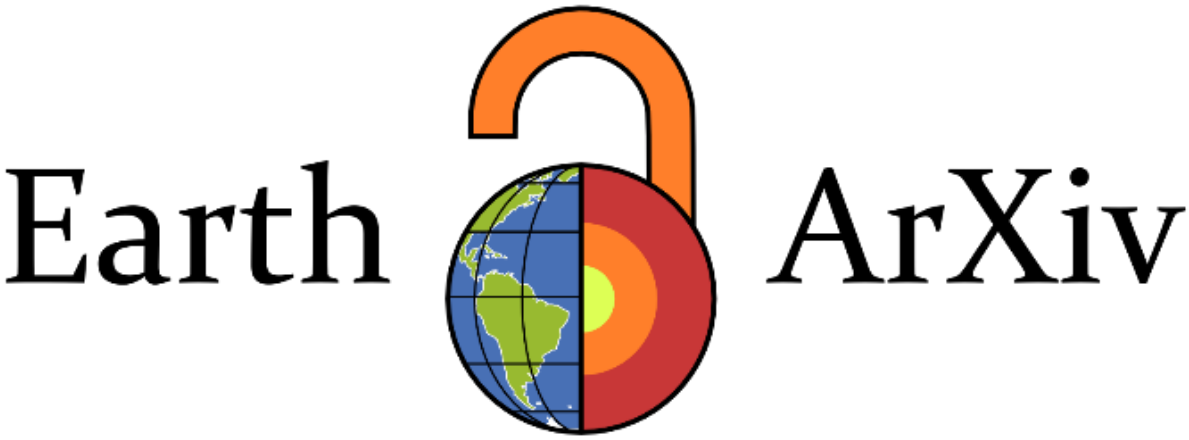

Beyond the 100-kyr and 41-kyr dichotomy: ~76- and ~52-kyr signals and forbidden periodicities in Quaternary glacial cycles

Takahito Mitsui

Faculty of Health Data Science, Juntendo University, Urayasu, Chiba 279-0013, Japan.

Email: takahito321@gmail.com

While the Mid-Pleistocene Transition (MPT) is often termed a shift from 41-kyr to ~100-kyr glacial cycles, this binary perspective fails to capture the nuanced spectral evolution of Quaternary climate. Using weighted wavelet spectral analysis of benthic δ^{18}O records, we identified previously underappreciated signals—~52 kyr before 1.2 Ma and ~76 kyr thereafter—marking the MPT's onset. These timescales primarily correspond to integer multiples (n) of the climatic precession period (T_p), with modulation by obliquity. We find that when T_p falls within an intermediate range (20.5–22 kyr), high eccentricity triggers deglaciation, precluding cycles of 60–65 kyr and 100–110 kyr. These findings refine the conventional dichotomy of the "41-kyr and 100-kyr worlds," revealing that the pre-MPT regime—~41-kyr but including ~52-kyr cycles—evolved into a post-MPT sequence of quantized ~76, ~95, and ~120-kyr cycles. Ultimately, our results restore precession-based pacing as a fundamental driver throughout the Quaternary, showing that glacial dynamics are consistently governed by the interplay between precession and obliquity.

INTRODUCTION

Glacial–interglacial cycles are the dominant mode of Quaternary climate variability, characterized by substantial fluctuations in temperature (*1, 2*), global ice volume (*3*), and atmospheric greenhouse gas concentrations (*4, 5*). Benthic oxygen isotope ratios (δ^{18}O) from marine sediments record past ice volume variations, although they are also influenced by deep-sea temperature and salinity (*6*) (Fig. 1d). Over the course of long-term Cenozoic cooling, the dominant periodicity of these cycles shifted from ~41 kyr to ~100 kyr, accompanied by an increase in amplitude—a reorganization known as the Mid-Pleistocene Transition (MPT; 1.25–0.7 Ma) (*7–9*).

While the astronomical influence on glacial cycles via insolation forcing was proposed as early as the mid-19th century, it lacked robust observational support until the late 20th century (*14*). Hays et al. (1976) (*15*) provided a breakthrough by performing spectral analysis of marine δ^{18}O records, identifying ~19- and ~23-kyr peaks corresponding to climatic precession (Fig. 1b) and a ~41-kyr peak corresponding to obliquity (Fig. 1a) (*10, 16*). This provided compelling evidence that glacial cycles are paced by orbital forcing. However, the ultimate pacemaker of the ~100-kyr cycles remains controversial; high-latitude summer insolation, considered crucial for the waxing and waning of continental ice sheets, lacks significant power within the ~100-kyr band (*14, 15*). Consequently, the ~100-kyr cycles are often interpreted as nonlinear responses occurring once every four or five precession cycles (*17–19*) or every two or three obliquity cycles (*20–22*). It remains a matter of active debate whether precession (*19, 23–26*), obliquity (*20, 21*), or a combination of both (*13, 22, 27–29*) predominantly governs their timing, rhythm, and amplitude.

Many studies have investigated the triggers of deglaciations by relating their timing to the phases of obliquity, precession, and various insolation metrics (*19, 22, 26, 27, 30*). However, uniquely defining the timing of deglaciations is inherently challenging, as the process sometimes spans multiple precession cycles and involves several discrete stages of ice-sheet retreat (see below). Although spectral analysis avoids these timing ambiguities, it often lacks the resolution required to distinguish spectral peaks necessary to address the precession-versus-obliquity debate at the ~100-kyr scale.

Here, we revisit the spectral analysis of glacial-interglacial cycles using a weighted wavelet spectral analysis method, originally developed by Foster (1996) as the Weighted Wavelet Z-

transform (*31*) and refined by Kirchner and Neal (2013) (*32*). This approach estimates spectral power via a localized weighted least-squares projection (see Materials and Methods). Implemented via the Python package `Pyleoclim` (*33*), this method resolves both the time-evolving nature of dominant periodicities (scalogram) and the overall power spectral density (PSD) without requiring prior interpolation or detrending. Beyond well-established spectral components, our analysis reveals a distinct ~76-kyr peak (post-1.25 Ma) and a 52-kyr power band (pre-1 Ma) across multiple benthic stacks—findings further corroborated by conventional spectral estimators. Drawing on the theoretical framework of Tzedakis et al. (2017) (*13*), we interpret these periodicities as robust evidence of nonlinear subharmonic (many-to-one) responses of glacial cycles to climatic precession forcing.

RESULTS

Weighted wavelet spectral analysis of benthic δ^{18}O records

We performed weighted wavelet spectral analysis on seven benthic δ^{18}O records (Fig. S1) to investigate their periodicities under varying age-modeling constraints (see Materials and Methods). First, we include the orbitally-tuned LR04 stack (*6*) (Fig. 1d) and its orbital-tuning-free counterpart in Lisiecki (2010) (*34*). Second, we analyze recent stack records in Zhou et al. (2026) (*35*): $\text{BIGSTACK}_{\text{mixed}}$ uses speleothem-based age constraints for 0–654 ka and tuning to an ice-sheet model for earlier intervals; $\text{BIGSTACK}_{\text{magrev}}$ is primarily constrained by paleomagnetic events to minimize orbital circularity; and $\text{BIGSTACK}_{\text{auto}}$ is generated using an automated optimization algorithm (*36*) to minimally tune to the pervasive 41-kyr obliquity cycle, while avoiding assumptions about astronomical phase relationships. Additionally, we utilize the orbitally-untuned benthic stack record in Huybers (2007) (*37*) and the paleomagnetically-constrained record U1476pMag from IODP Site U1476 (*25*). To ensure the robustness of the detected periodicities, we primarily focus on results from records with minimal or no orbital tuning (Lisiecki 2010, $\text{BIGSTACK}_{\text{magrev}}$, Huybers 2007, and U1476pMag), while using the fully tuned records as supplementary evidence.

The result of time-frequency analysis for the orbitally tuned LR04 record is shown in Fig. 1e, with the yellow line tracking the instantaneous period at which the wavelet amplitude is maximized

(see Figs. S2–S7 for the other records). The evolution of the dominant period in the seven records compared in Fig. 2 exhibits a broadly similar pattern across all analyzed records, although the MPT epoch (0.7–1.25 Ma) is notably complex, with marked discrepancies between records.

Prior to the MPT, the dominant period remains centered near 41 kyr, although most records show transient increases in the primary period between 1.8 and 2.1 Ma (Fig. 2), with some variability in timing among the stacks. At the onset of the MPT, the dominant period increases up to ~76 kyr by ~1.2 Ma, a feature robust across records. However, this increase is interrupted around 1.1 Ma, and the subsequent evolution of the dominant period during 1.1–0.7 Ma varies significantly among the records. Notably, the dominant period retreats to ~22 kyr in the tuned and untuned LR04 records and to ~41 kyr in the other records at least once during 1.1–0.9 Ma. This transient reduction in period coincides with the strongest eccentricity maximum of the Quaternary. While the emergence of strong ~100-kyr power after ~700 ka is well documented (*38–40*), our analysis uncovers a more nuanced progression. Specifically, the dominant period remains centered near ~95 kyr over 700–300 ka, after which it lengthens toward ~120 kyr (Fig. 2). The temporal evolution of the dominant period of ice age cycles closely follows that of eccentricity, excluding the ~400-kyr component, suggesting the establishment of frequency locking between ice volume and ~100-kyr-scale eccentricity cycles after the end of the MPT (~700 ka) (Fig. 2c).

To assess the statistical significance of the observed periodicities, we calculated power spectral densities (PSDs) for the intervals before and after the MPT. For the mid-to-late Pleistocene (the past 1.25 Myr), 95-kyr, 41-kyr, and 23-kyr periodicities generally exhibit significant power at the 95% confidence level, although the latter two do not reach this level in the U1476 record (Fig. 3). Notably, we identify a spectral peak near ~76 kyr, which is significant in all records—including the orbitally tuned LR04 (at the 90% level) and U1476—except for the untuned LR04. However, conventional periodograms (Fig. S9) reveal significant ~76-kyr peaks across all records, including the untuned LR04. While this peak is less defined in Lomb–Scargle periodograms over the last 1.25 Myr, it becomes significant when the analysis is extended to the full Quaternary (2.6 Myr) except the untuned LR04 (Fig. S10). During the early-to-mid Pleistocene (1.0–2.6 Ma), the 41-kyr spectral peak is prominent across all records (Fig. 4). The tuned LR04 record further exhibits a significant peak at ~52 kyr, while the PSDs of $\text{BIGSTACK}_{\text{magrev}}$ and Huybers (2007) show a significant shoulder extending from the 41-kyr peak toward this periodicity. A similar, though non-significant

(< 95%), feature is present in the untuned LR04. In contrast, no comparable 52-kyr power is observed in $\text{BIGSTACK}_{\text{mixed}}$, $\text{BIGSTACK}_{\text{auto}}$, and U1476pMag. Given that $\text{BIGSTACK}_{\text{auto}}$ and $\text{BIGSTACK}_{\text{magrev}}$ share the same δ^{18}O values but employ different age-modeling strategies, it is possible that the ~52-kyr power was suppressed or lost during the orbital tuning process to the 41-kyr obliquity cycles. Regarding U1476pMag, the absence of ~52-kyr power likely stems from its relatively short record length (786.5 kyr), which limits the spectral resolution required to resolve such components. Consistently, alternative estimators—specifically conventional (Fig. S9) and Lomb-Scargle periodograms (Fig. S10)—detect the ~52-kyr feature in most records, reinforcing its robust presence.

In summary, spectral power near ~76 kyr and ~52 kyr is reproducible across multiple datasets and estimation methods, though detectability varies with age modeling and tuning strategies. The ~76-kyr peak is a consistent feature of late Pleistocene variability, while the ~52-kyr feature—despite less consistent expression—appears to be a real component of early-to-mid Pleistocene variability rather than an analytical artifact. The lack of detection in the untuned LR04 likely reflects its conservative age constraints using only three tie points over the 2.6 Myr (*34*) (Materials and Methods), which may dampen these specific periodicities.

Interpretation of ~76-kyr and ~52-kyr components

We interpret the periodicities detected in the PSD in relation to insolation cycles, using the theoretical framework of interglacial spacing proposed by Tzedakis et al. (2017) (*13*) (T17). In this model, an interglacial occurs when the caloric summer half-year insolation peak at 65°N exceeds a threshold that declines with the time elapsed since the previous interglacial, reflecting the accumulated instability during the glacial period (Materials and Methods). Using this criterion, the model predicts which insolation peaks lead to interglacials over the Quaternary (Fig. 1, vertical dashed lines). Though BIGSTACK was recently published (*35*) as an update to LR04, we use LR04 in the following analysis because the T17 model was calibrated using that stack.

We calculate proxy-based deglaciation spacings and insolation-based interglacial spacings, demonstrating their overall consistency. Following T17, interglacials are identified in the LR04 record when δ^{18}O values fall below a predefined threshold (see Materials and Methods). Near

each threshold-crossing timing of δ^{18}O, the timing of deglaciation is specified as the peak in the derivative of the 10-kyr smoothed LR04 δ^{18}O record (Figs. S11–S13). Some deglaciations span multiple precession cycles, leaving multiple peaks in δ^{18}O derivative (e.g., deglaciations leading to MIS 13a near 500 ka as well as MIS 17 near 700 ka in Fig. S11). We select the largest derivative peak within a window of either ±10 kyr or ±15 kyr around each threshold-crossing point. The ±10-kyr window tends to capture the later peak within a deglaciation sequence, whereas the ±15-kyr window captures the earlier peak (Figs. S11–S13). The resulting spacings between deglaciations, denoted T_{later} and T_{earlier}, are shown in Fig. 5. Furthermore, we define insolation-based interglacial spacing (T_{ins}) as the intervals between successive caloric summer insolation peaks that ultimately induced each interglacial (*13*) (Fig. 5; Fig. 1e, green dots). The δ^{18}O-derivative-based intervals may tightly couple with the periodicities detected in the PSD, but their values rely on an assumed age model. In contrast, the insolation-based intervals are relatively free from chronological uncertainties and can be directly linked to orbital cycles. See Supplementary Data S1 for the values of T_{later}, T_{earlier}, and T_{ins}.

The high consistency among T_{later}, T_{earlier}, and T_{ins} shown in Fig. 5a ($r \gtrsim 0.95$, RMSE $\lesssim 6.5$ kyr) supports T_{ins} as a reliable basis for analyzing glacial-cycle periodicities. Although discrepancies of up to ~20 kyr exist for certain deglaciations—likely reflecting the inherent uncertainty in deglaciation timing and the simplified nature of the T17 model—the overall robustness of the correlation supports using T_{ins} for interpreting the periodicities in the PSD.

The distribution of T_{ins} shows clear clustering around 90–93 kyr and 73–76 kyr (Fig. 5e). A similar, albeit weaker, clustering is preserved in T_{earlier} (Fig. 5d). We, therefore, attribute the ~95-kyr spectral peak to the cluster of 90–93 kyr spacings, and the ~76-kyr spectral peak to the 73–76 kyr cluster. Before the MPT (~1.2 Ma), T_{ins} is distributed around the 41-kyr obliquity period with a mean of 41.2 kyr, contributing to the dominant 41-kyr peak. However, its standard deviation is substantial (±10 kyr). Indeed, four spacings fall within 51–53 kyr (Figs. 1e, 5e), contributing to the significant ~52-kyr peak in the PSD of the LR04 record over 1.0–2.6 Ma (Fig. 4a).

Once linked with T_{ins}, the observed spectral peaks can be traced back to their physical origins by decomposing the insolation forcing into climatic precession and obliquity components. A key factor in considering the variability of T_{ins} is that the duration of climatic precession cycles varies widely between 14 and 31 kyr when eccentricity is low, whereas it remains relatively stable around

22.1 kyr when eccentricity is high (Fig. S14) (*42*). Indeed, the length of the late-Pleistocene glacial cycles is explained with the varying durations of climatic precession cycles (*19*). Building on this, we derive more refined relationships between T_{ins} and the evolving durations of precession and obliquity cycles.

For each glacial cycle, we approximate the local variations in the caloric summer half-year insolation as $f(t) = A_p \cos(\omega_p t + \varphi_p) + A_o \cos(\omega_o t + \varphi_o)$, accounting for the respective positive contributions of climatic precession and obliquity to the insolation. Here, $A_{p,o}$ are the local-mean amplitudes, $\omega_{p,o}$ are the angular frequencies (corresponding to local-mean periods $T_{p,o}$), and $\varphi_{p,o}$ are the local phases of climatic precession and obliquity cycles. Unless otherwise noted, we can choose $A_{p,o} = 1$ for 65°N caloric summer insolation, as climatic precession and obliquity contribute nearly equally to the total variance (*11*). The local-mean periods T_p (T_o) are calculated from the time intervals between successive precession minima (obliquity maxima) associated with deglaciations (Figs. S15–S18; Data S1). The local phases $\varphi_{p,o}$ are chosen from the discrete set $\{0, \pm\pi/2, \pi\}$ for simplicity, to best capture local insolation variations. Then, we obtain approximation formulae for T_{ins} as follows.

Here we present two representative cases (all derivations are provided in the Supplementary text). When the peaks of climatic precession and obliquity nearly coincide and collectively induce an interglacial, we define this peak time as $t = 0$ by setting $\varphi_p = \varphi_o = 0$ (Fig. S19a). If the spacing T_{ins} between the peak at $t = 0$ and a subsequent interglacial-inducing peak is close to the n-th multiple of the local-mean precession period T_p, it can be expressed as $T_{\mathrm{ins}} = nT_p + \delta$. Here, δ represents a small temporal shift relative to the nominal insolation peak, originating from the modulation by obliquity. By linearizing the peak condition as $f'(nT_p + \delta) \approx f'(nT_p) + f''(nT_p)\delta = 0$, we obtain approximation formule for T_{ins} ($n = 2, 3, 4, 5$), called type-a:

$$T_{\mathrm{ins}} \approx nT_p - \frac{A_o \omega_o \sin(n\omega_o T_p)}{A_p \omega_p^2 + A_o \omega_o^2 \cos(n\omega_o T_p)}.$$

An example of type-a is the ~76-kyr spacing between interglacials MIS 11c and MIS 9e (Fig. S15), where the corresponding insolation peaks are separated by approximately four precession cycles ($n = 4$), and the local-mean precession period is $T_p = 18.25$ kyr. Furthermore, the local-mean obliquity period is $T_o = 41.5$ kyr. The type-a formula then predicts $T_{\mathrm{ins}} = 74.3$ kyr. This value is closer to the actual value of 76 kyr than the simple multiple of precession, $nT_p = 73$ kyr, obtained

without the shift $\delta = 1.43$ kyr.

The second case occurs when a glacial cycle spans roughly three precession cycles ($n = 3$); here, the insolation is locally approximated as $f(t) = -A_p \cos(\omega_p t) - A_o \cos(\omega_o t)$ over the interval $-\frac{3}{2}T_p \lesssim t \lesssim \frac{3}{2}T_p$ corresponding to $\varphi_p = \varphi_o = \pi$ (Fig. S19b). For this case, we assume that deglaciations occur at $t = \pm(\frac{3}{2}T_p + \delta)$, with δ being a small obliquity-induced shift. Following a derivation similar to that of the type-a formulae, $T_{\rm ins}$ is given by the following formula (type-3b):

$$T_{\rm ins} \approx 3T_p + \frac{2A_o\omega_o \sin\left(\frac{3}{2}\omega_o T_p\right)}{A_p\omega_p^2 - A_o\omega_o^2 \cos\left(\frac{3}{2}\omega_o T_p\right)}.$$

An example of type-3b is the spacing between interglacials MIS 37 and MIS 35 (Fig. S16). The corresponding insolation peaks are separated by approximately three precession cycles, and the local-mean precession period is $T_p = 19$ kyr. Furthermore, the local-mean obliquity period is $T_o = 39$ kyr. Then, the type-3b formula predicts $T_{\rm ins} = 54.2$ kyr. This value is closer to the actual value of 53 kyr than the simple multiple of precession, $nT_p = 57$ kyr, obtained without the shift $\delta = -2.8$ kyr.

In this manner, by varying the number of precession cycles (n) and the local phases $\varphi_{p,o}$, we derive twelve distinct formulae (e.g., types 2a–5a, 1b–4b, 1c–2c, 2d, and pp). The detailed derivation of each formula is presented in the Supplementary text, along with a one-to-one correspondence to each individual glacial cycle (Table S1). These analytical expressions account for nearly 50 interglacial spacings identified throughout the Quaternary. While we generally use a fixed amplitude ratio of $A_p/A_o = 1$ for simplicity, we explicitly consider the relative amplitudes in two specific cases of extremely low eccentricity (MIS 99–97 and MIS 97–95). Similarly, the intervals MIS 95–93 and MIS 93–91 represent epochs in which eccentricity remains near zero. The aforementioned formulae are inapplicable to these events as deglaciation aligns with the obliquity maximum at 2386 ka, where eccentricity is virtually zero. For these two cases, we employ exceptional but simplified estimates for $T_{\rm ins}$, the details of which are described in the Supplementary text. The validity of this analytical framework is confirmed by its high predictive power; across the entire Quaternary, these formulae approximate $T_{\rm ins}$ with a mean absolute error of only 0.8 kyr (Fig. 5b).

Precession phase-locking and forbidden periodicities

It is found that the shift δ in the approximation $T_{\mathrm{ins}} = nT_p + \delta$ has standard deviation of only 2.7 kyr. Consequently, the insolation-based interglacial spacings T_{ins} cluster along the lines $T_{\mathrm{ins}} = nT_p$ (n = 1, 2, 3, 4, 5) as functions of the local-mean precession period T_p (Fig. 6a). The number of precession cycles within each interglacial spacing, n, can be explained by the T17 theory (*13*), where a longer spacing $T_{\mathrm{ins}} (\approx nT_p)$ facilitates crossing the deglaciation threshold due to the accumulated instability of the ice sheet–climate system (see Materials and Methods). After the onset of the MPT around 1.2 Ma, n statistically increases as a result of an elevated deglaciation threshold, and the points (T_p, T_{ins}) tend to cluster along higher branches with $n \geq 3$.

Figure 6a reveals that similar interglacial spacings (T_{ins}) can arise from different precession-cycle lengths (T_p). For instance, the 90–93 kyr spacings comprise either four precession cycles with a mean period of $T_p \approx 23$ kyr or five cycles with a mean period of $T_p \approx 19$ kyr. Similarly, the 73–76-kyr spacings comprise either three precession cycles with a mean period of $T_p \approx 24$ kyr or four precession cycles with a mean period of $T_p \approx 19$ kyr. A similar bifurcation is observed for the 51–53-kyr spacings, which split into two distinct solutions: three multiples of precession cycles with a mean period of $T_p \approx 19$ kyr and two multiples of precession cycles with a mean period of $T_p \approx 26.5$ kyr. The points in ~41-kyr cluster distribute along $T_{\mathrm{ins}} = 2T_p$ (Fig. 6a, the second dashed line from the bottom), showing the persistent influence of precession cycles across the MPT, as suggested in previous studies (*25, 43–45*).

Interestingly, when the mean climatic precession period T_p falls between 20.5 and 22 kyr, glacial cycles longer than 50 kyr are notably absent (shaded region, Fig. 6a). This gap occurs because this intermediate T_p range coincides with periods of high mean eccentricity ($\overline{e} > 0.04$) both after and, in many cases, before the MPT's onset (~1.2 Ma) (Fig. 6b). Under these conditions of high eccentricity, the amplified climatic precession forcing ensures that summer insolation remains sufficiently high to trigger deglaciation within one or two precession cycles (Fig. 6c), thereby precluding longer cycles. This orbital constraint provides a physical basis for the distinct gaps observed in the spacing histograms (Figs. 5c–5e), explaining why certain durations—~60–66 kyr (3×20 to 3×22) and ~100–110 kyr (5×20 to 5×22)—are effectively precluded.

DISCUSSION

We show that glacial cycles evolved from a quasi-41-kyr regime characterized by large variability—including ~52-kyr cycles—to quantized ~76, ~95, and ~120-kyr cycles. This points to precession-based pacing as a persistent feature of glacial dynamics throughout the Quaternary. Following the onset of the MPT (~1.2 Ma), ~76-kyr cycles emerged, coinciding with the disappearance of the ~52-kyr periodicity. After the first ~92-kyr cycle appeared at ~0.9 Ma, the dominant period stabilized around ~95 kyr from ~700 to ~300 ka, before eventually lengthening toward ~120 kyr. This temporal evolution of the dominant period closely tracks the ~100-kyr eccentricity component (excluding the 400-kyr cycle), suggesting that frequency-locking between ice volume and eccentricity was established after the end of the MPT (~700 ka; Fig. 2c). Such resonance between the internal climate response and orbital forcing may explain the abrupt increase in 100-kyr cycle amplitude observed at approximately 650 ka (*38*).

While the prominence of the ~76-kyr periodicity has been noted in several studies (*19, 46, 47*), its physical origin has remained elusive. For instance, Bolton et al. (1995) (*46*) identified ~75-kyr power around 750 ka but attributed it to internal variability, citing the lack of a corresponding periodicity in the astronomical forcing. Rial (1999) (*47*) proposed that the ~75-kyr peak is a sideband frequency ($1/77 \approx 1/95 + 1/413$) generated by frequency modulation of the 95-kyr cycle by the 413-kyr eccentricity component; however, the physical basis for such modulation remains elusive. In contrast, our results demonstrate that the ~76-kyr spectral power arises from subharmonic phase-locking to either three precession cycles (mean period $T_p \approx 24$ kyr) or four precession cycles ($T_p \approx 19$ kyr), with minor modulation by obliquity. Consistently, Blackburn et al. (2024) (*19*) attributed the spacings from MIS 13a to 11c and 11c to 9e to the 76-kyr mode of four precession cycles. This precession-based 76-kyr mode is distinct from the previously proposed ~70-kyr variability, which was interpreted as a beat frequency between obliquity and eccentricity ($1/70 \approx 1/41 - 1/100$) (*41*). Within our present framework, the ~95-kyr spectral power can also be explained as a result of subharmonic phase-locking to either four ($T_p \approx 23$ kyr) or five ($T_p \approx 19$ kyr) precession cycles (*17–19, 23, 26, 48*).

While the dominant power prior to the MPT is often characterized as ~41 kyr (*49*), this represents only a statistical average. In reality, interglacial spacings exhibit large variations of ~10

kyr around this mean because they correspond to either two or three multiples of climatic precession cycles, whose periods themselves vary significantly. Such variability in glacial duration is indeed reproduced in a mathematical model or a climate-ice sheet model (*44, 50*). Our analysis identifies the ~52-kyr-scale spectral shoulder extending from the 41-kyr peak as a diagnostic signature of this precessional influence prior to the onset of the MPT (~1.2 Ma). Previous research (*41*) attributed the spectral peaks near 50 kyr and 55 kyr to an eccentricity overtone ($1/50 = 2/100$ kyr^{-1}) and an obliquity sideband, respectively. In contrast, we focus on the 51–53 kyr band and attribute its origin to a nonlinear subharmonic response. This is characterized by two distinct solutions: the system responding once for every three precessional cycles of a mean period of $T_p \approx 19$ kyr or once for every two cycles of a mean period of $T_p \approx 26.5$ kyr.

The presence of bundles of precession cycles—~52-kyr cycles before ~1.2 Ma, ~76-kyr cycles after ~1.2 Ma, and ~95-kyr cycles after ~0.9 Ma—throughout the Pleistocene suggests that the MPT was not a disappearance of the obliquity-driven 41-kyr world, but rather a progressive shift in the skipping behavior of precession-paced deglaciations. This persistent influence of precession cycles both before and after the MPT is consistent with recent findings (*25, 43–45, 51*).

Consequently, the MPT can be understood as a period-adding process in precession phase-locking, driven by a gradual increase in the deglaciation threshold in the coupled ice-sheet–ocean–carbon system. The threshold likely increased gradually through long-term global cooling, declining atmospheric CO_2 toward critical minima (*52–54*), and structural changes in the cryosphere system including progressive removal of subglacial regolith beneath Northern Hemisphere ice sheets (*54–56*), expansion of marine-based Antarctic ice sheets (*57*), long-term AMOC slowdown (*58*), and enhanced stratification of the Southern Ocean (*59*). These processes may have contributed to increasing the intrinsic timescale of the climate–ice-sheet system (*28, 60*), although their relative roles and interactions remain poorly constrained. Identifying the underlying physical mechanisms of the MPT is beyond the scope of this study.

We found that when the local-mean precession period T_p falls within this intermediate range (20.5–22 kyr), high eccentricity triggers deglaciation, precluding the emergence of ~100–110-kyr and ~60–65-kyr cycles. This is consistent with previous findings of an anticorrelation between ~100-kyr eccentricity power and ~100-kyr ice-age power (*44, 61*). Our analysis shows that mean eccentricity does not exceed 0.04 during the observed ~100-kyr cycles (Fig. 6c). This implies that

the development of ~100-kyr cycles was precluded during the high-eccentricity interval between ~950 and 1100 ka. Consequently, the onset of the MPT—specifically the lengthening of glacial cycles—appears to have been constrained by the long-term evolution of eccentricity (*9, 44*).

Our findings refine the conventional paradigm of a simple transition from a 41-kyr world to a 100-kyr world across the MPT. Instead, we propose a more nuanced evolution: from a quasi-41-kyr regime characterized by high orbital variability to a suite of quantized cycles (~76, ~95, and ~120 kyr) linked to precession phases. In this framework, obliquity determines which climatic precession peaks are skipped, as suggested in several studies (*13, 19, 27, 28*).

MATERIALS AND METHODS

Benthic δ^{18}O records

We analyze seven benthic δ^{18}O records (Fig. S1) categorized by their degree of orbital tuning. The first is the standard, orbitally-tuned LR04 stack (*6*) (Fig. 1d). The second is the tuning-free version of the LR04 stack from Lisiecki (2010) (*34*), which assumes a constant sedimentation rate between three primary tie points: the core top (0 ka) and the geomagnetic reversals at 0.78 and 2.58 Ma. Third through fifth, we utilize three versions of the BIGSTACK from Zhou et al. (2026) (*35*): $\text{BIGSTACK}_{\text{mixed}}$ integrates 221 global records using speleothem-based age constraints for 0–654 ka and ice-sheet model tuning for earlier intervals. $\text{BIGSTACK}_{\text{magrev}}$ (comprising 33 records) is constrained by 15 paleomagnetic events over the last 2.606 Ma to minimize orbital circularity. $\text{BIGSTACK}_{\text{auto}}$ is derived from $\text{BIGSTACK}_{\text{magrev}}$ by applying the eTimeOpt algorithm (*36, 62*) to minimally tune the pervasive 41-kyr obliquity signal without assuming astronomical phase relationships. The sixth record is the depth-derived stack of Huybers (2007) (*37*). While the original study focuses on the last 2 Ma, the dataset provides a tuning-free chronology anchored to the 2.58 Ma geomagnetic boundary (`https://doi.org/10.25921/d1zr-t492`, last accessed 8 April 2026). Lastly, we include the single-site benthic δ^{18}O record from IODP Site U1476, anchored to an independent paleomagnetic age model (U1476pMag) (*25*). Because this record spans only the last 1786.542 kyr, its coverage of the pre-MPT interval (1.0–1.79 Ma) is relatively short. Consequently, the presence or absence of periodicities in this specific epoch should be interpreted with caution

due to the limited duration of the time series.

In our spectral analysis, periodicities are primarily accepted based on the tuning-free records (Lisiecki 2010, Huybers 2007, and U1476pMag) and the minimally-tuned $\text{BIGSTACK}_{\text{magrev}}$. The orbitally-tuned records (standard LR04, $\text{BIGSTACK}_{\text{mixed}}$, and $\text{BIGSTACK}_{\text{auto}}$) are used as supplementary evidence to support the robustness of the detected signals.

Weighted wavelet spectral analysis

Paleoclimate time series are commonly unevenly sampled, which complicates the application of conventional spectral estimators, such as the periodogram (*63*) and the multitaper method spectrum (*64*). Standard approaches often rely on interpolation to a regular time grid prior to analysis; however, such interpolation acts as a low-pass filter, leading to a reddening of the power spectrum and, consequently, spurious results in hypothesis testing (*65*). While the Lomb–Scargle periodogram (*66,67*) avoids interpolation, it is known to overestimate power at high frequencies (*65*). Moreover, Fourier-based methods, which assume stationarity, necessitate data detrending (*68*). However, even with recent methodological advances, identifying and removing a trend without inadvertently compromising the underlying climate signal remains an inherently difficult task (*69*).

To overcome these difficulties, we employ a weighted wavelet spectral analysis method. This approach, originally developed by Foster (1996) (*31*) as the Weighted Wavelet Z-transform (WWZ) and subsequently refined by Kirchner and Neal (2013) (*32*), estimates spectral power via weighted least-squares projection. This approach, implemented in the Python package `Pyleoclim` (*33*), enables the resolution of both the time-evolving nature of dominant periodicities (scalograms) and the overall frequency content (power spectral density; PSD) without requiring prior interpolation or detrending.

The method estimates time-dependent harmonic amplitudes (a_1, a_2) through localized fits of sinusoidal functions and a constant to the data using weighted least squares (*32*). Specifically, for each center time t^* and angular frequency ω, the coefficients a_1 and a_2 are obtained by fitting: $x_i = a_0 + a_1 \cos[\omega(t_i - t^*)] + a_2 \sin[\omega(t_i - t^*)]$, where each observation x_i at time t_i is weighted by a Gaussian weight $w_i = \exp[-c\omega^2(t_i - t^*)^2]$, with a decay constant c controlling the time-frequency resolution trade-off. However, when the data are unevenly sampled in time, the basis functions

can be non-orthogonal (e.g., $\sum_i \cos[\omega(t_i - t^*)] \sin[\omega(t_i - t^*)] \neq 0$), which can lead to significant errors in estimating the coefficients. To address this, Kirchner and Neal (2013) employ shifted basis functions such that: $x_i = b_0 + b_1 \cos[\omega(t_i - \tau)] + b_2 \sin[\omega(t_i - \tau)]$, where the time shift τ is chosen to ensure that the basis functions 1, $\cos[\omega(t_i - \tau)]$, and $\sin[\omega(t_i - \tau)]$ are mutually orthogonal. The coefficients b_0, b_1, and b_2 obtained via weighted regression are then converted back to the original coefficients a_0, a_1, and a_2 by accounting for the phase shift $\omega(t^* - \tau)$.

The local spectral power, or scalogram, is calculated at each t^* as: $S_{\text{loc}}(t^*, \omega) = \frac{1}{2}(a_1^2 + a_2^2)(t_{\max} - t_{\min})\frac{n_{\text{eff}}}{n}$, where $t_{\max} - t_{\min}$ is the total time interval covered by the n samples, and $n_{\text{eff}} = (\sum_i w_i)^2 / \sum_i w_i^2$ represents the effective number of points. Finally, a robust global estimate of the Power Spectral Density (PSD) is obtained by averaging the local spectral power over the entire time interval, as $S(\omega) = \sum_{t^*} v_{\text{eff}}(t^*) S_{\text{loc}}(t^*, \omega) / \sum_{t^*} v_{\text{eff}}(t^*)$, where $v_{\text{eff}}(t^*) = \max\{0, n_{\text{eff}} - 3\}$ is the effective degrees of freedom (*32*).

The decay constant c determines the frequency resolution in the spectral analysis and balances the frequency and time resolution in the time-frequency analysis. For the time-frequency analysis (scalogram), we adopt $c = 1/(8\pi^2)$, the standard value for this analysis in `Pyleoclim` (*33*), which provides a balanced resolution for identifying transient shifts in ice age periodicity. For the global spectral analysis (PSD), we set $c = 0.0005$. This corresponds to a broader effective time window (slightly smaller than the default value 0.001 in `Pyleoclim`) to prioritize high frequency resolution.

To check the sensitivity of our results, we conduct spectral analyses using multiple estimators: the conventional periodogram (*63*) and the Lomb-Scargle periodogram (*66, 67*). For the former, the time series is interpolated at 1-kyr intervals. In both cases, the series are linearly detrended over the analysis period. All analyses are performed using the `pyleoclim` (version 1.2.0) (*33*).

Interglacial spacings in Tzedakis et al. (2017)

Tzedakis et al. (2017) proposed a simple rule to determine which insolation peaks trigger interglacials (*13*). In their model, 51 interglacials are identified over the Quaternary based on the LR04 benthic δ^{18}O stack (*6*), supported by additional composite records from Eastern Equatorial Pacific sites. An interglacial onset is defined when the detrended δ^{18}O value falls below a lower threshold of 3.68 after having exceeded a higher threshold of 3.92 . To apply this criterion consistently, δ^{18}O

values prior to 1.5 Ma are detrended as $\delta^{18}O_{\text{detrended}} = \delta^{18}O + 3.296 \times 10^{-4}(t - 1500)$, where t is the time in kyr, while values after 1.5 Ma remain unchanged. This trend is attributed to the long-term cooling of deep-water temperatures or an increase in Antarctic ice volume.

The T17 model predicts interglacial onsets based on caloric summer half-year insolation. This measure represents the total insolation integrated over the caloric summer half-year, which is defined such that every day within this period receives more insolation than any day in the winter half (*11, 12*). At 65°N, the variance of this insolation measure receives approximately equal contributions from climatic precession and obliquity. In the T17 framework, an interglacial is triggered when a peak in the 65°N caloric summer insolation exceeds a threshold that decreases as a function of the time elapsed since the previous interglacial (Δt), reflecting the accumulation of glacial instability. This condition can be expressed as the effective energy, defined as $E(I_{\text{peak}}, \Delta t) = I_{\text{peak}} + b\Delta t$, exceeding a constant deglaciation threshold $I_{\text{threshold}}$. Here, $b = 0.0021 \pm 0.0001$ GJ m^{-2} kyr^{-1}, and $I_{\text{threshold}}$ is defined to ramp up from 6.02 GJ m^{-2} to 6.14 GJ m^{-2} over the interval from 1.55 Ma to 0.61 Ma. Using this criterion, the model can predict most of 51 interglacial onsets, with only two false negatives (MIS 59 and 63). For these false negatives, the insolation peaks immediately preceding their respective isotopic minima are assumed to be the trigger. In the present work, the interglacial spacings (T_{ins}) are defined as the durations between successive caloric summer insolation peaks that finally induced each interglacial. Using the T17, the interglacial spacing T_{ins} is determined as the minimal peak-to-peak spacing that satisfies the condition $E(I_{\text{peak}}, T_{\text{ins}}) = I_{\text{peak}} + bT_{\text{ins}} > T_{\text{threshold}}$. Therefore, $n = \text{argmin}_{\tilde{n} \geq 1}\{I_{\text{peak}} + b(\tilde{n}T_p + \delta) > T_{\text{threshold}}\}$.

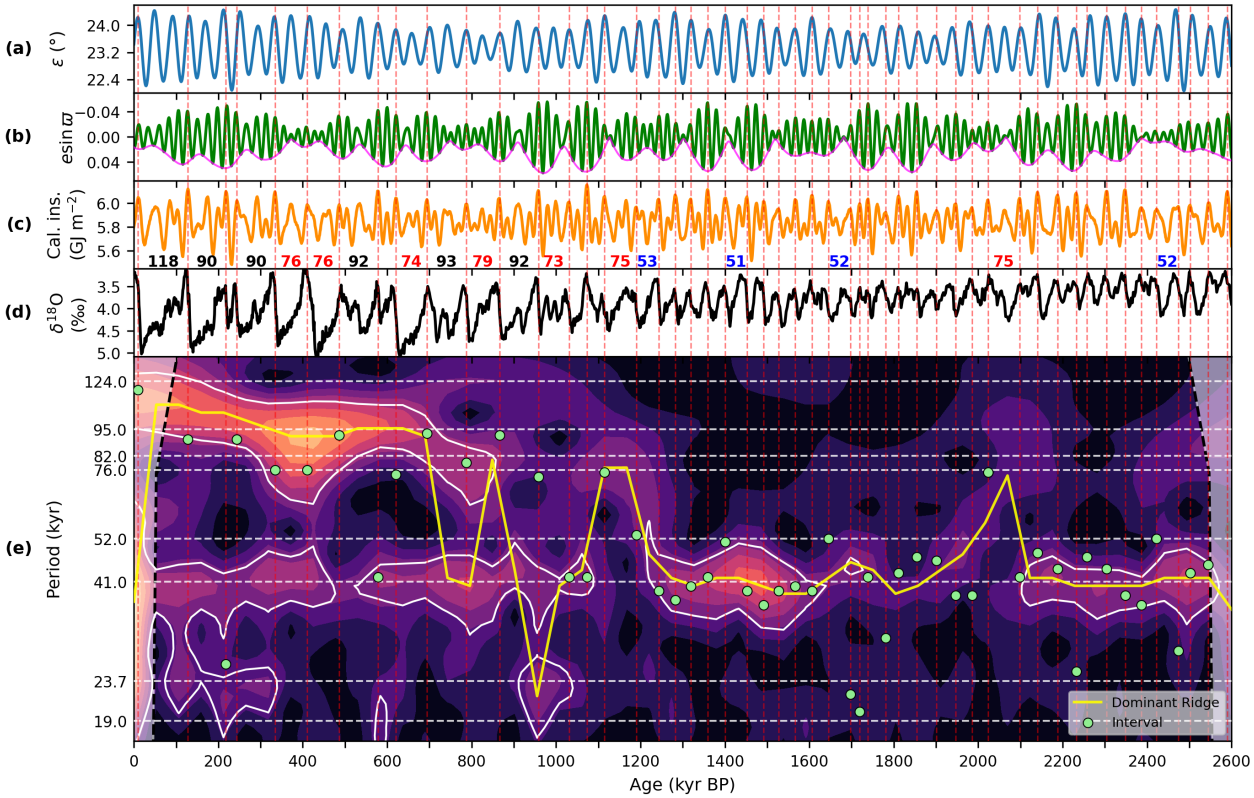

Figure 1: **Orbital forcing and wavelet analyses of the LR04 benthic δ^{18}O stack record over the last 2.6 Myr.** (a) Obliquity (ε) (*10*). (b) Climatic precession ($e \sin \varpi$, green) and its eccentricity envelope (e, magenta) (*10*). Note that negative values of climatic precession correspond to positive anomalies in Northern Hemisphere summer insolation. (c) Caloric summer half-year insolation at 65°N (*11, 12*). (d) LR04 benthic δ^{18}O stack record (*6*). Higher δ^{18}O values indicate larger ice volume and lower deep-ocean temperatures. (e) Wavelet power scalogram of the δ^{18}O record. The yellow line indicates the ridge of maximum wavelet power. Areas enclosed by white dashed lines indicate power significant at the 95% confidence level against an AR(1) benchmark. Horizontal dashed lines denote major astronomical periodicities, including the 76-kyr and 52-kyr scales discussed in this study. The vertical dashed lines indicate the timings of insolation peaks associated with interglacial onsets, as defined in Tzedakis et al. (2017) (*13*), across all panels. Spacings longer than 50 kyr between successive interglacial-inducing insolation peaks are labeled in panel (c). In panel (e), the green dots indicate the insolation-based interglacial spacing (T_{ins}) derived from these peaks.

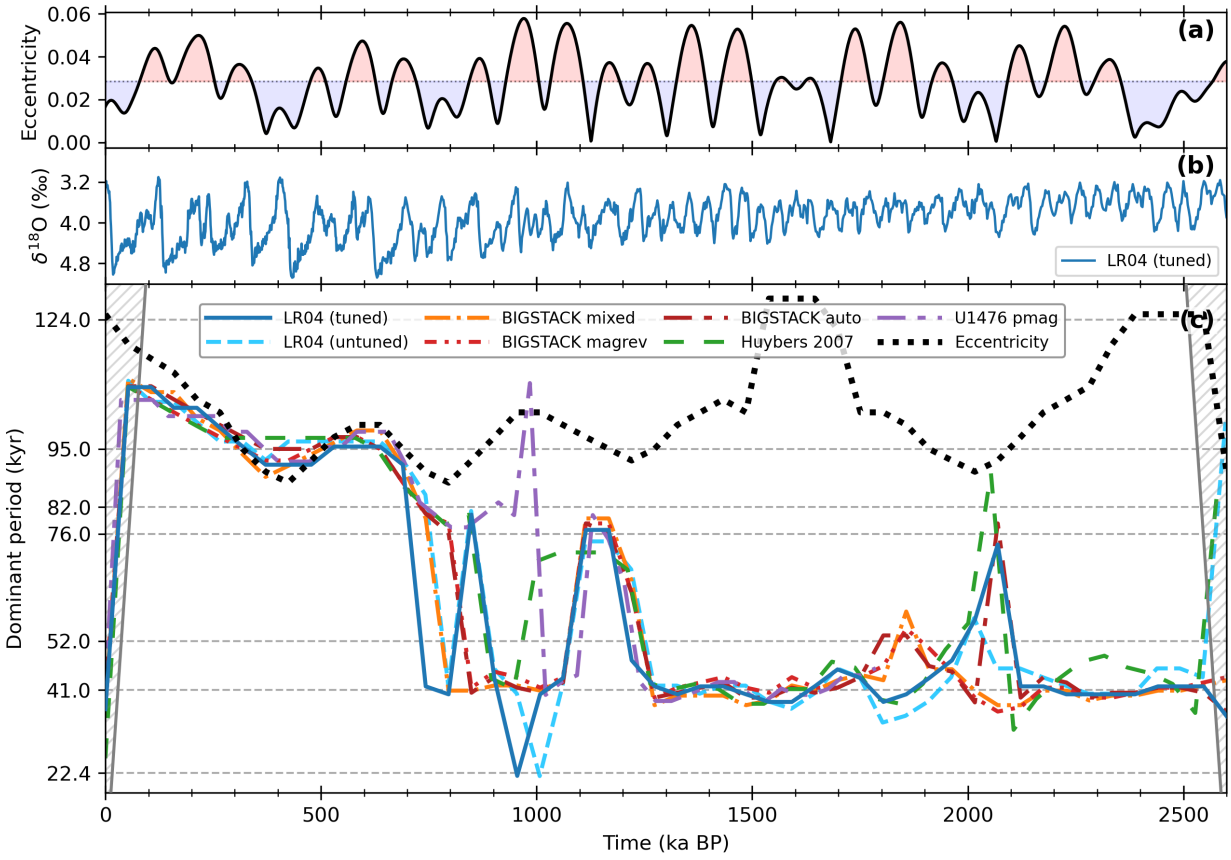

Figure 2: **Evolution of the dominant timescale of glacial cycles and that of eccentricity.** (a) Eccentricity. The horizontal is the average. (b) LR04 benthic δ^{18}O stack. (c) Dominant timescale corresponding to the maximum wavelet amplitude at each time. Horizontal dashed lines denote major astronomical periodicities, including the 76-kyr and 52-kyr scales discussed in this study.

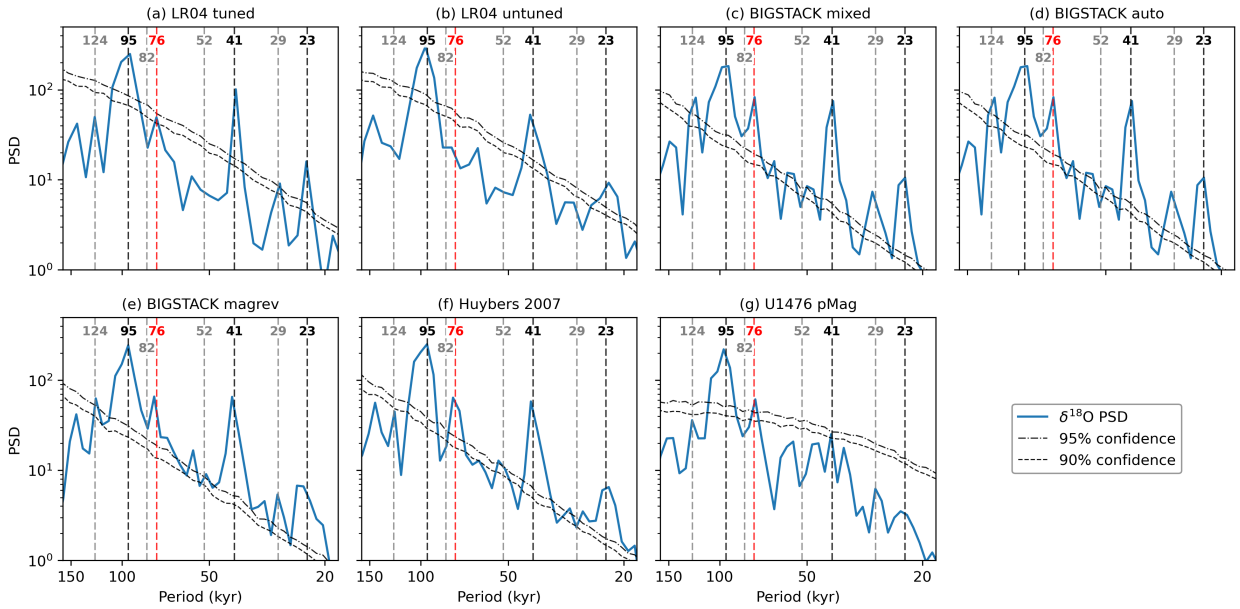

Figure 3: **Power spectral densities (PSD) of benthic δ^{18}O records over the last 1.25 Myr.** (a) the tuned LR04 stack (*6*), (b) the untuned LR04 stack (*34*), (c) BIGSTACK$_{\text{mixed}}$ (*35*), (d) BIGSTACK$_{\text{auto}}$ (*35*), (e) BIGSTACK$_{\text{magrev}}$ (*35*), (f) the untuned record from Huybers (2007) (*37*), and (g) the U1476 record (*25*). Solid blue lines denote the PSD of the δ^{18}O records, and dashed/dotted black lines indicate the 95% and 90% confidence levels against an AR(1) benchmark. Vertical dashed lines highlight key periodicities: eccentricity (124 and 95 kyr), obliquity (41 kyr), and climatic precession (23 kyr). Also indicated are the subharmonic of 41 kyr (82 kyr), the combination tone (29 kyr; $1/29 \approx 1/41 + 1/95$) (*41*), and specific timescales of interest in this study (76 and 52 kyr).

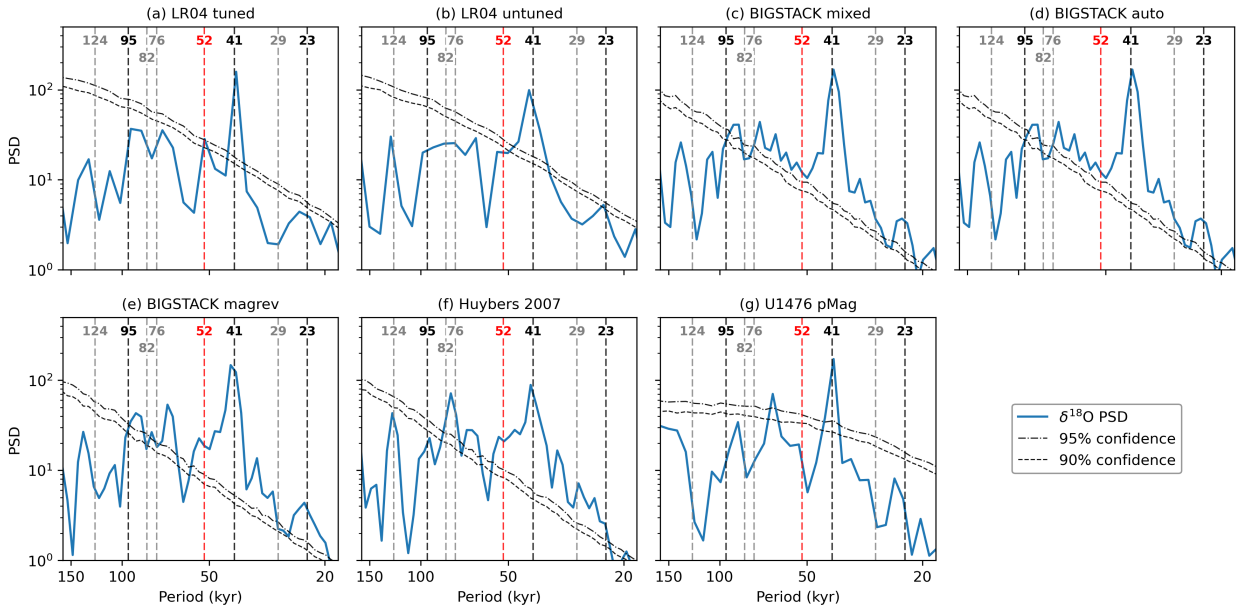

Figure 4: **Power spectral densities (PSD) of benthic δ^{18}O records over 1.0–2.6 Ma.** (a) the tuned LR04 stack (*6*), (b) the untuned LR04 stack (*34*), (c) BIGSTACK$_{\text{mixed}}$ (*35*), (d) BIGSTACK$_{\text{auto}}$ (*35*), (e) BIGSTACK$_{\text{magrev}}$ (*35*), (f) the untuned record from Huybers (2007) (*37*), and (g) the U1476 record (*25*). Solid blue lines denote the PSD of the δ^{18}O records, and dashed/dotted black lines indicate the 95% and 90% confidence levels against an AR(1) benchmark. Vertical dashed lines highlight key periodicities: eccentricity (124 and 95 kyr), obliquity (41 kyr), and climatic precession (23 kyr). Also indicated are the subharmonic of 41 kyr (82 kyr), the combination tone (29 kyr; $1/29 \approx 1/41 + 1/95$) (*41*), and specific timescales of interest in this study (76 and 52 kyr).

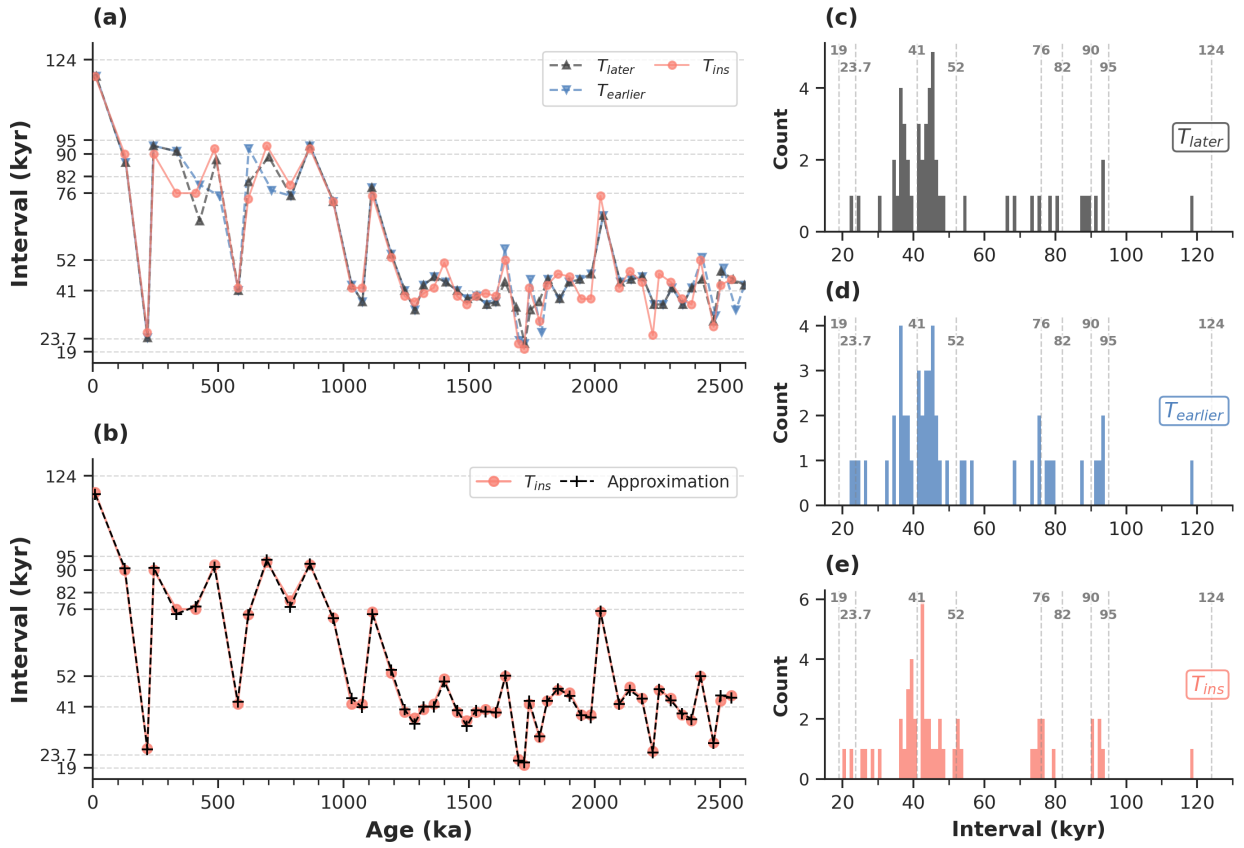

Figure 5: **Comparison of proxy-based deglaciation spacings and insolation-based interglacial spacings.** (a) Time series of spacings over the past 2600 kyr. These intervals are defined by three different metrics: orbital insolation peaks (T_{ins}, salmon circles) and the timing of peak deglaciation rates (T_{later}, dark blue triangles; T_{earlier}, light blue inverted triangles). Horizontal dashed lines indicate key orbital periodicities and the sub-harmonic periodicities discussed in this study (52, 76, and 82 kyr). (b) Comparison between the insolation-based spacings (T_{ins}) and their theoretical approximation (black crosses). (c)–(e) Frequency distributions (histograms) of (c) T_{later}, (d) T_{earlier}, and (e) T_{ins}. The insolation-based distribution (e) exhibits distinct clustering around 73–76 kyr and 90–93 kyr; this pattern is partially reflected in the T_{earlier} and T_{later} metrics. All proxy-based metrics align well with T_{ins} ($r \gtrsim 0.95$, RMSE $\lesssim 6.5$ kyr), justifying the use of T_{ins} as a robust theoretical framework for spectral analysis.

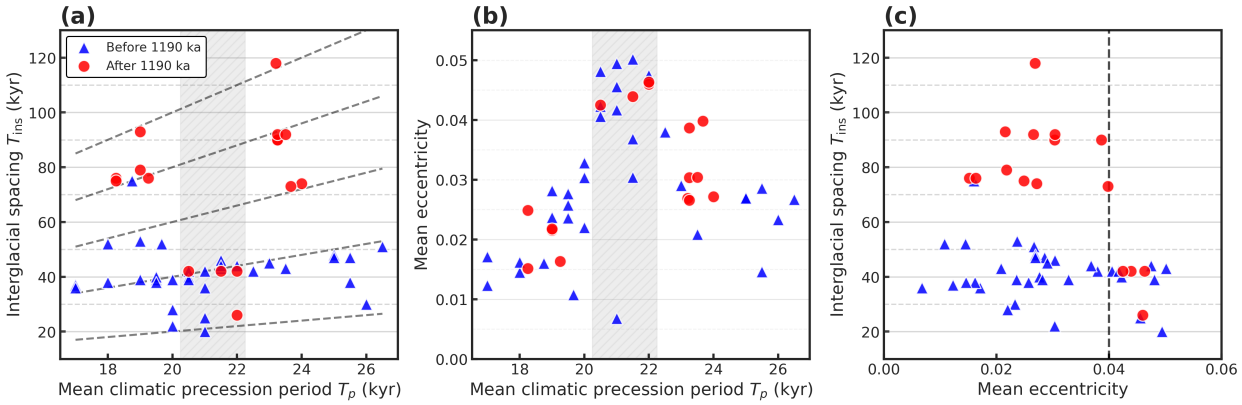

Figure 6: **Orbital constraints on interglacial spacing and the role of eccentricity.** (a) Mean climatic precession period (T_p) versus the insolation-based interglacial spacing (T_{ins}). T_p is defined as the average duration of climatic precession cycles within each interglacial spacing. Dashed lines represent integer multiples of T_p ($T_{\text{ins}} = nT_p$ for $n = 1, \ldots, 5$), showing the clustering of interglacial spacing. (b) T_p versus the mean eccentricity ($\bar{e}$), averaged over the full duration of each interglacial spacing. In (a) and (b), the vertical hatched area (20.25–22.25 kyr) indicates the range of T_p where high mean eccentricity generally precludes glacial cycles longer than 50 kyr. (c) Mean eccentricity versus T_{ins}. The vertical dashed line at $\bar{e} = 0.04$ indicates the threshold above which high eccentricity constrains T_{ins} to values below 50 kyr by facilitating deglaciation. In all panels, blue triangles and red circles represent intervals before and after 1190 ka, respectively.

References and Notes

1. P. U. Clark, J. D. Shakun, Y. Rosenthal, P. Köhler, P. J. Bartlein, Global and regional temperature change over the past 4.5 million years. *Science* **383** (6685), 884–890 (2024).

2. J. Jouzel, *et al.*, Orbital and millennial Antarctic climate variability over the past 800,000 years. *science* **317** (5839), 793–796 (2007).

3. E. J. Rohling, *et al.*, Comparison and synthesis of sea-level and deep-sea temperature variations over the past 40 million years. *Reviews of Geophysics* **60** (4), e2022RG000775 (2022).

4. D. Lüthi, *et al.*, High-resolution carbon dioxide concentration record 650,000–800,000 years before present. *Nature* **453** (7193), 379–382 (2008).

5. L. Loulergue, *et al.*, Orbital and millennial-scale features of atmospheric CH4 over the past 800,000 years. *Nature* **453** (7193), 383–386 (2008).

6. L. E. Lisiecki, M. E. Raymo, A Pliocene-Pleistocene stack of 57 globally distributed benthic δ18O records. *Paleoceanography* **20** (1) (2005).

7. T. D. Herbert, The mid-Pleistocene climate transition. *Annual Review of Earth and Planetary Sciences* **51** (1), 389–418 (2023).

8. C. J. Berends, P. Köhler, L. J. Lourens, R. S. W. van de Wal, On the Cause of the Mid-Pleistocene Transition. *Reviews of Geophysics* **59** (2), e2020RG000727 (2021), e2020RG000727 2020RG000727, doi:https://doi.org/10.1029/2020RG000727.

9. E. L. McClymont, S. M. Sosdian, A. Rosell-Melé, Y. Rosenthal, Pleistocene sea-surface temperature evolution: Early cooling, delayed glacial intensification, and implications for the mid-Pleistocene climate transition. *Earth-Science Reviews* **123**, 173–193 (2013).

10. J. Laskar, *et al.*, A long-term numerical solution for the insolation quantities of the Earth. *Astronomy & Astrophysics* **428** (1), 261–285 (2004).

11. M. Milankovitch, Kanon der erdbestahlung und seine anwendung auf das eiszeitproblem, 133. *Königlich Serbische Academie, Belgrade* (1941).

12. M. Crucifix, Palinsol: insolation for palaeoclimate studies, R package version 0.93 (2016).

13. P. Tzedakis, M. Crucifix, T. Mitsui, E. W. Wolff, A simple rule to determine which insolation cycles lead to interglacials. *Nature* **542** (7642), 427–432 (2017).

14. D. Paillard, Glacial cycles: toward a new paradigm. *Reviews of Geophysics* **39** (3), 325–346 (2001).

15. J. D. Hays, J. Imbrie, N. J. Shackleton, Variations in the Earth's Orbit: Pacemaker of the Ice Ages. *Science* **194** (4270), 1121–1132 (1976).

16. A. Berger, Support for the astronomical theory of climatic change. *Nature* **269** (5623), 44–45 (1977).

17. M. Raymo, The timing of major climate terminations. *Paleoceanography* **12** (4), 577–585 (1997).

18. A. J. Ridgwell, A. J. Watson, M. E. Raymo, Is the spectral signature of the 100 kyr glacial cycle consistent with a Milankovitch origin? *Paleoceanography* **14** (4), 437–440 (1999).

19. T. Blackburn, S. Kodama, G. Piccione, Eccentricity paces late Pleistocene glaciations. *Geophysical Research Letters* **51** (12), e2024GL108751 (2024).

20. P. Huybers, C. Wunsch, Obliquity pacing of the late Pleistocene glacial terminations. *Nature* **434** (7032), 491–494 (2005).

21. K. H. Nyman, P. D. Ditlevsen, The middle Pleistocene transition by frequency locking and slow ramping of internal period. *Climate Dynamics* **53** (5), 3023–3038 (2019).

22. P. Bajo, *et al.*, Persistent influence of obliquity on ice age terminations since the Middle Pleistocene transition. *Science* **367** (6483), 1235–1239 (2020).

23. A. Abe-Ouchi, *et al.*, Insolation-driven 100,000-year glacial cycles and hysteresis of ice-sheet volume. *Nature* **500** (7461), 190–193 (2013).

24. H. Cheng, *et al.*, The Asian monsoon over the past 640,000 years and ice age terminations. *nature* **534** (7609), 640–646 (2016).

25. S. Barker, *et al.*, Persistent influence of precession on northern ice sheet variability since the early Pleistocene. *Science* **376** (6596), 961–967 (2022).

26. B. Hobart, L. E. Lisiecki, D. Rand, T. Lee, C. E. Lawrence, Late Pleistocene 100-kyr glacial cycles paced by precession forcing of summer insolation. *Nature Geoscience* **16** (8), 717–722 (2023).

27. P. Huybers, Combined obliquity and precession pacing of late Pleistocene deglaciations. *Nature* **480** (7376), 229–232 (2011).

28. T. Mitsui, M. Willeit, N. Boers, Synchronization phenomena observed in glacial-interglacial cycles simulated in an Earth system model of intermediate complexity. *Earth System Dynamics* **2023**, 1277–1294 (2023), doi:10.5194/esd-14-1277-2023, `https://doi.org/10.5194/esd-14-1277-2023`.

29. T. Mitsui, P. C. Tzedakis, E. W. Wolff, Insolation evolution and ice volume legacies determine interglacial and glacial intensity. *Climate of the Past* **18** (9), 1983–1996 (2022).

30. S. Barker, L. E. Lisiecki, G. Knorr, S. Nuber, P. C. Tzedakis, Distinct roles for precession, obliquity, and eccentricity in Pleistocene 100-kyr glacial cycles. *Science* **387** (6737), eadp3491 (2025).

31. G. Foster, Time series analysis by projection. I. Statistical properties of Fourier analysis. *Astronomical Journal v. 111, p. 541* **111**, 541 (1996).

32. J. W. Kirchner, C. Neal, Universal fractal scaling in stream chemistry and its implications for solute transport and water quality trend detection. *Proceedings of the National Academy of Sciences* **110** (30), 12213–12218 (2013).

33. D. Khider, *et al.*, Pyleoclim: Paleoclimate timeseries analysis and visualization with Python. *Paleoceanography and Paleoclimatology* **37** (10), e2022PA004509 (2022).

34. L. Lisiecki, A benthic δ13C-based proxy for atmospheric pCO2 over the last 1.5 Myr. *Geophysical Research Letters* **37** (21) (2010).

35. Y. Zhou, L. E. Lisiecki, S. R. Meyers, T. Lee, C. Lawrence, Global and regional Pleistocene benthic δ 18 O stacks with a comparison of different age modeling strategies. *Geochronology* **8** (1), 85–107 (2026).

36. S. R. Meyers, The evaluation of eccentricity-related amplitude modulation and bundling in paleoclimate data: An inverse approach for astrochronologic testing and time scale optimization. *Paleoceanography* **30** (12), 1625–1640 (2015).

37. P. Huybers, Glacial variability over the last two million years: an extended depth-derived agemodel, continuous obliquity pacing, and the Pleistocene progression. *Quaternary Science Reviews* **26** (1-2), 37–55 (2007).

38. M. Mudelsee, K. Stattegger, Exploring the structure of the mid-Pleistocene revolution with advanced methods of time-series analysis. *Geologische Rundschau* **86** (2), 499–511 (1997).

39. P. U. Clark, *et al.*, The middle Pleistocene transition: characteristics, mechanisms, and implications for long-term changes in atmospheric pCO2. *Quaternary Science Reviews* **25** (23-24), 3150–3184 (2006).

40. L. E. Lisiecki, M. E. Raymo, Plio–Pleistocene climate evolution: trends and transitions in glacial cycle dynamics. *Quaternary Science Reviews* **26** (1-2), 56–69 (2007).

41. P. Huybers, C. Wunsch, A depth-derived Pleistocene age model: Uncertainty estimates, sedimentation variability, and nonlinear climate change. *Paleoceanography* **19** (1) (2004).

42. P. Huybers, O. Aharonson, Orbital tuning, eccentricity, and the frequency modulation of climatic precession. *Paleoceanography* **25** (4) (2010).

43. P. R. Liautaud, D. A. Hodell, P. J. Huybers, Detection of significant climatic precession variability in early Pleistocene glacial cycles. *Earth and Planetary Science Letters* **536**, 116137 (2020).

44. Y. Watanabe, *et al.*, Astronomical forcing shaped the timing of early Pleistocene glacial cycles. *Communications Earth & Environment* **4** (113) (2023).

45. D. Liebrand, A. de Bakker, Bispectra of climate cycles show how ice ages are fuelled. *Climate of the Past* **15** (6), 1959–1983 (2019).

46. E. W. Bolton, K. A. Maasch, J. M. Lilly, A wavelet analysis of Plio-Pleistocene climate indicators: A new view of periodicity evolution. *Geophysical Research Letters* **22** (20), 2753–2756 (1995).

47. J. A. Rial, Pacemaking the ice ages by frequency modulation of Earth's orbital eccentricity. *Science* **285** (5427), 564–568 (1999).

48. H. Cheng, *et al.*, Ice age terminations. *Science* **326** (5950), 248–252 (2009).

49. M. E. Raymo, K. H. Nisancioglu, The 41 kyr world: Milankovitch's other unsolved mystery. *Paleoceanography* **18** (1) (2003).

50. E. Legrain, F. Parrenin, E. Capron, A gradual change is more likely to have caused the Mid-Pleistocene Transition than an abrupt event. *Communications Earth & Environment* **4** (1), 90 (2023).

51. S. T. Kodama, T. Blackburn, Eccentricity controls the magnitude and periodicity of Pleistocene glacial cycles. *Paleoceanography and Paleoclimatology* **41** (3), e2026PA005420 (2026).

52. B. Hönisch, N. G. Hemming, D. Archer, M. Siddall, J. F. McManus, Atmospheric carbon dioxide concentration across the mid-Pleistocene transition. *Science* **324** (5934), 1551–1554 (2009).

53. T. B. Chalk, *et al.*, Causes of ice age intensification across the Mid-Pleistocene Transition. *Proceedings of the National Academy of Sciences* **114** (50), 13114–13119 (2017).

54. M. Willeit, A. Ganopolski, R. Calov, V. Brovkin, Mid-Pleistocene transition in glacial cycles explained by declining CO2 and regolith removal. *Science Advances* **5** (4), eaav7337 (2019).

55. M. Yehudai, *et al.*, Evidence for a Northern Hemispheric trigger of the 100,000-y glacial cyclicity. *Proceedings of the National Academy of Sciences* **118** (46), e2020260118 (2021).

56. P. U. Clark, D. Pollard, Origin of the middle Pleistocene transition by ice sheet erosion of regolith. *Paleoceanography* **13** (1), 1–9 (1998).

57. Z. An, *et al.*, Mid-Pleistocene climate transition triggered by Antarctic Ice Sheet growth. *science* **385** (6708), 560–565 (2024).

58. C. Basak, *et al.*, Southern Hemisphere initiation of the mid-Pleistocene transition. *Science Advances* **12** (10), eaea6811 (2026).

59. S. K. Hines, *et al.*, Revisiting the mid-Pleistocene transition ocean circulation crisis. *Science* **386** (6722), 681–686 (2024).

60. T. Mitsui, P. Ditlevsen, N. Boers, M. Crucifix, 100 kyr ice age cycles as a timescale-matching problem. *Earth System Dynamics* **16** (5), 1569–1584 (2025).

61. L. E. Lisiecki, Links between eccentricity forcing and the 100,000-year glacial cycle. *Nature geoscience* **3** (5), 349–352 (2010).

62. S. R. Meyers, Cyclostratigraphy and the problem of astrochronologic testing. *Earth-Science Reviews* **190**, 190–223 (2019).

63. P. Bloomfield, *Fourier analysis of time series: an introduction* (John Wiley & Sons) (2004).

64. D. J. Thomson, Spectrum estimation and harmonic analysis. *Proceedings of the IEEE* **70** (9), 1055–1096 (1982).

65. M. Schulz, M. Mudelsee, REDFIT: estimating red-noise spectra directly from unevenly spaced paleoclimatic time series. *Computers & Geosciences* **28** (3), 421–426 (2002).

66. N. R. Lomb, Least-squares frequency analysis of unequally spaced data. *Astrophysics and space science* **39** (2), 447–462 (1976).

67. J. D. Scargle, Studies in astronomical time series analysis. II-Statistical aspects of spectral analysis of unevenly spaced data. *Astrophysical Journal, Part 1, vol. 263, Dec. 15, 1982, p. 835-853.* **263**, 835–853 (1982).

68. Z. Wu, N. E. Huang, S. R. Long, C.-K. Peng, On the trend, detrending, and variability of nonlinear and nonstationary time series. *Proceedings of the National Academy of Sciences* **104** (38), 14889–14894 (2007).

69. F. Zhu, *et al.*, Climate models can correctly simulate the continuum of global-average temperature variability. *Proceedings of the National Academy of Sciences* **116** (18), 8728–8733 (2019).

70. K. H. Nisancioglu, Plio-pleistocene glacial cycles and milankovitch variability. *Elements of Physical Oceanography: A derivative of the Encyclopedia of Ocean Sciences* p. 344 (2009).

Acknowledgments

The author thanks Prof. Polychronis Tzedakis and Prof. Eric W. Wolff for insightful communications that inspired this work.

Funding: This work was supported by JSPS KAKENHI Grant Number 26K00011.

Competing interests: The author declares no competing interests.

Data and materials availability: The one-to-one correspondence between each glacial cycle and the insolation-based interglacial spacing (Table S1) is provided in `Data_S1_formula.xlsx` at `https://doi.org/10.5281/zenodo.19534114`. All the other data used in this study are publicly available from the original sources cited in the main text and Supplementary materials.

Supplementary materials

Supplementary Text

Figs. S1 to S19

Tables S1

Supplementary Materials for

Beyond the 100-kyr and 41-kyr dichotomy: ~76- and ~52-kyr signals and forbidden periodicities in Quaternary glacial cycles

Takahito Mitsui*

*Corresponding author. Email: takahito321@gmail.com

This PDF file includes:

Supplementary Text

Figs. S1 to S18

Tables S1

Other Supplementary Materials for this manuscript:

Electronic version of Table S1: `Data_S1_formula.xlsx` available at

`https://doi.org/10.5281/zenodo.19534114`

Supplementary text

Derivation of the approximation formulae of interglacial spacings

Following Tzedakis et al. (2017) (*13*), we assume that each interglacial onset can be linked with a specific peak in the caloric summer half-year insolation at 65°N (*11, 12*). Thus, the insolation-based interglacial spacings (T_{ins}) are defined between successive caloric summer half-year insolation peaks that finally induced each interglacial (*13*) (Figs. S11a–S13a). Here we derive approximate formulae for T_{ins} of each glacial cycle based on local information on climatic precession and obliquity (*10*) (Fig. S15–S18).

It is known that the caloric summer half-year insolation, especially at 65°N, is well approximated by a superposition of standardized indices of climatic precession and obliquity (*11, 70*). Since the climatic precession oscillates more rapidly than obliquity, the insolation peak closest to the deglaciation isotopic change is more tightly linked with a climatic precession peak (minimum). Indeed, the link between the length of glacial cycles and the durations of astronomical cycles—particularly precession—has been noted in various studies (*19, 23, 24, 26*). On the other hand, the duration of climatic precession cycles varies widely (between 14 and 31 kyr) when eccentricity is low, whereas it remains relatively stable around 22.1 kyr when eccentricity is high (Fig. S14) (*19, 42*). Building on this, we here derive finer relationships between T_{ins} and the evolving durations of precession and obliquity cycles.

For each glacial cycle, we approximate the local variations in the caloric summer half-year insolation as $f(t) = A_p \cos(\omega_p t + \varphi_p) + A_o \cos(\omega_o t + \varphi_o)$, accounting for the respective positive contributions of climatic precession and obliquity to the insolation. Here, $A_{p,o}$ are the local-mean amplitudes, $\omega_{p,o}$ are the angular frequencies (corresponding to local-mean periods $T_{p,o}$), and $\varphi_{p,o}$ are the local phases of climatic precession and obliquity cycles. Note that the maxima of $A_p \cos(\omega_p t + \varphi_p)$ correspond to the minima of the climatic precession cycles, as precession minima contribute to maximal insolation. Then, we can derive analytical expressions for T_{ins}. A complete correspondence between individual glacial cycles and their respective formulae is provided in Table S1.

Formula type 2a, 3a, 4a and 5a. When the peaks of climatic precession and obliquity nearly coincide and collectively induce an interglacial, we define this peak time as $t = 0$ by setting

$\varphi_p = \varphi_o = 0$ (Fig. S19a). If the spacing T_{ins} between the peak at $t = 0$ and a subsequent interglacial-inducing peak is close to the n-th multiple of the local-mean precession period T_p, it can be expressed as $T_{\mathrm{ins}} = nT_p + \delta$, where the small shift δ reflects the phase modulation by obliquity. By linearizing the peak condition $f'(nT_p + \delta) = 0$ as $f'(nT_p + \delta) \approx f'(nT_p) + f''(nT_p)\delta = 0$, we obtain approximation formulae for T_{ins} ($n = 2,\ 3,\ 4,\ 5$), called type-a:

$$T_{\mathrm{ins}} \approx nT_p - \frac{A_o\omega_o \sin(n\omega_o T_p)}{A_p\omega_p^2 + A_o\omega_o^2 \cos(n\omega_o T_p)}.$$

An example of type-a is the ~76-kyr spacing between interglacials MIS 11c and MIS 9e (Fig. S15), where the corresponding insolation peaks are separated by approximately four precession cycles ($n = 4$), and the local-mean precession period is $T_p = 18.25$ kyr. Furthermore, the local-mean obliquity period is $T_o = 41.5$ kyr. The type-a formula then predicts $T_{\mathrm{ins}} = 74.3$ kyr. This value is closer to the actual value of 76 kyr than the simple multiple of precession, $nT_p = 73$ kyr, obtained without the shift $\delta = 1.43$ kyr.

Formulae type 1b and 3b. The second case occurs when a glacial cycle spans roughly one or three precession cycles (i.e., $n = 1$ or 3), with the insolation locally approximated as $f(t) = -A_p \cos(\omega_p t) - A_o \cos(\omega_o t)$ over the interval $-\frac{n}{2}T_p \lesssim t \lesssim \frac{n}{2}T_p$ (corresponding to $\varphi_p = \varphi_o = \pi$). For this case, we assume that deglaciations occur at $t = \pm(\frac{n}{2}T_p + \delta)$, with δ being a small obliquity-induced shift. By linearizing the peak condition $f'(\frac{n}{2}T_p + \delta) \approx f'(\frac{n}{2}T_p) + f''(\frac{n}{2}T_p)\delta = 0$, we obtain approximation formulae for T_{ins} ($n = 1,\ 3$), called type-1b or 3b:

$$T_{\mathrm{ins}} \approx nT_p + \frac{2A_o\omega_o \sin\left(\frac{n}{2}\omega_o T_p\right)}{A_p\omega_p^2 - A_o\omega_o^2 \cos\left(\frac{n}{2}\omega_o T_p\right)}.$$

An example of type-3b is the spacing between interglacials MIS 37 and MIS 35 (Fig. S16). The corresponding insolation peaks are separated by approximately three precession cycles ($n = 3$), and the local-mean precession period is $T_p = 19$ kyr. Furthermore, the local-mean obliquity period is $T_o = 39$ kyr. Then, the type-3b formula predicts $T_{\mathrm{ins}} = 54.2$ kyr. This value is closer to the actual value of 53 kyr than the simple multiple of precession, $nT_p = 57$ kyr, obtained without the shift $\delta = -2.8$ kyr.

Formulae type 2b. Consider a case where a glacial cycle spans approximately two precession cycles, in which the central precession peak is counteracted by an obliquity minimum, while the outer precession peaks are enhanced by adjacent obliquity maxima. This situation is approximated

as $f(t) = A_p \cos(\omega_p t) - A_o \cos(\omega_o t)$ over the interval $-T_p \lesssim t \lesssim T_p$ (corresponding to $\varphi_p = 0$ and $\varphi_o = \pi$). In a similar manner to the derivation of the formulae type-1b and 3b, T_{ins} is given by formula called type-2b:

$$T_{\text{ins}} \approx 2T_p + \frac{2A_o\omega_o \sin\left(\omega_o T_p\right)}{A_p\omega_p^2 - A_o\omega_o^2 \cos\left(\omega_o T_p\right)}.$$

Formulae type 4b. Consider a case where a glacial cycle spans approximately four precession cycles, in which the central precession peak is enhanced by an obliquity maximum, while the outer precession peaks are also enhanced by adjacent obliquity maxima. This situation is approximated as $f(t) = A_p \cos(\omega_p t) + A_o \cos(\omega_o t)$ over the interval $-2T_p \lesssim t \lesssim 2T_p$ (corresponding to $\varphi_p = \varphi_o = 0$). In a similar manner to the derivation of the formulae type-2b, T_{ins} is given by formula called type-4b:

$$T_{\text{ins}} \approx 4T_p - \frac{2A_o\omega_o \sin\left(2\omega_o T_p\right)}{A_p\omega_p^2 + A_o\omega_o^2 \cos\left(2\omega_o T_p\right)}.$$

Formulae type 1c and 2c. Consider a case where a glacial cycle spans roughly one or two precession cycles ($n = 1$ or 2), with the insolation locally approximated as $f(t) = A_p \cos(\omega_p t) - A_o \sin(\omega_o t)$ over the interval $0 \le t \lesssim nT_p$ (corresponding to $\varphi_p = 0$ and $\varphi_o = \frac{\pi}{2}$). In this case, the deglaciations occur at $t = 0$ and $t = nT_p + \delta$, where δ is a small shift. By linearizing the peak condition $f'(nT_p + \delta) \approx f'(nT_p) + f''(nT_p)\delta = 0$, we obtain approximation formulae for T_{ins} ($n = 1,\ 2$), called type-1c or 2c:

$$T_{\text{ins}} \approx nT_p - \frac{A_o\omega_o \cos\left(n\omega_o T_p\right)}{A_p\omega_p^2 - A_o\omega_o^2 \sin\left(n\omega_o T_p\right)}.$$

Formula 2d. Consider a case where a glacial cycle spans roughly two precession cycles, with the insolation locally approximated as $f(t) = A_p \cos(\omega_p t) + A_o \sin(\omega_o t)$ over the interval $0 \le t \lesssim 2T_p$ (corresponding to $\varphi_p = 0$ and $\varphi_o = -\frac{\pi}{2}$). In this case, the deglaciations occur at $t = 0$ and $t = 2T_p + \delta$, where δ is a small shift. By linearizing the peak condition $f'(2T_p + \delta) \approx f'(2T_p) + f''(2T_p)\delta = 0$, we obtain the approximation formula for T_{ins}, called type-2d:

$$T_{\text{ins}} \approx 2T_p + \frac{A_o\omega_o \cos\left(2\omega_o T_p\right)}{A_p\omega_p^2 - A_o\omega_o^2 \sin\left(2\omega_o T_p\right)}.$$

Formula type pp. In this case, the interglacial spacing is primarily determined by the spacing between precession peaks; while obliquity cycles may shift the timing of both deglaciations, they do so by the same amount, leaving the net spacing almost unchanged. Therefore,

$$T_{\text{ins}} \approx nT_p.$$

Choice of amplitude $A_{p,o}$. Climatic precession and obliquity contribute nearly equally to the total variance in the caloric summer half-year insolation at 65°N (*11, 12*). Therefore, for simplicity, we set $A_{p,o} = 1$ for 65°N caloric summer half-year insolation except for the following two cycles. However, the cycle from MIS 99 to 97 as well as the cycle from MIS 97 to 95 are characterized by low eccentricity (i.e., low precession amplitude) and high obliquity amplitude. Assessing their variances locally, we took $A_o/A_p = 3$ and $A_o/A_p = 2.5$ for the former and the latter, respectively.

Two exceptions The spacings MIS 95–93 and MIS 93–91 represent epochs during which eccentricity remains near zero. The aforementioned formulae are inapplicable to these events because deglaciation coincides with the obliquity maximum at 2386 ka, where eccentricity is virtually zero. For these cases, we adopt simplified estimates for T_{ins}. The MIS 95–93 interval is assumed to be initiated by an insolation peak occurring midway between the obliquity maximum at 2426 ka and the precession minimum at 2419 ka, and is finalized by the obliquity maximum at 2386 ka. Consequently, the spacing is estimated as $(2426 + 2419)/2 - 2386 = 36.5$ kyr. Similarly, the MIS 93–91 interval is initiated by the 2386-ka obliquity maximum and finalized by an insolation peak midway between the obliquity maximum at 2348 ka and the precession minimum at 2347 ka. The spacing is thus estimated as $2386 - (2348 + 2347)/2 = 38.5$ kyr.

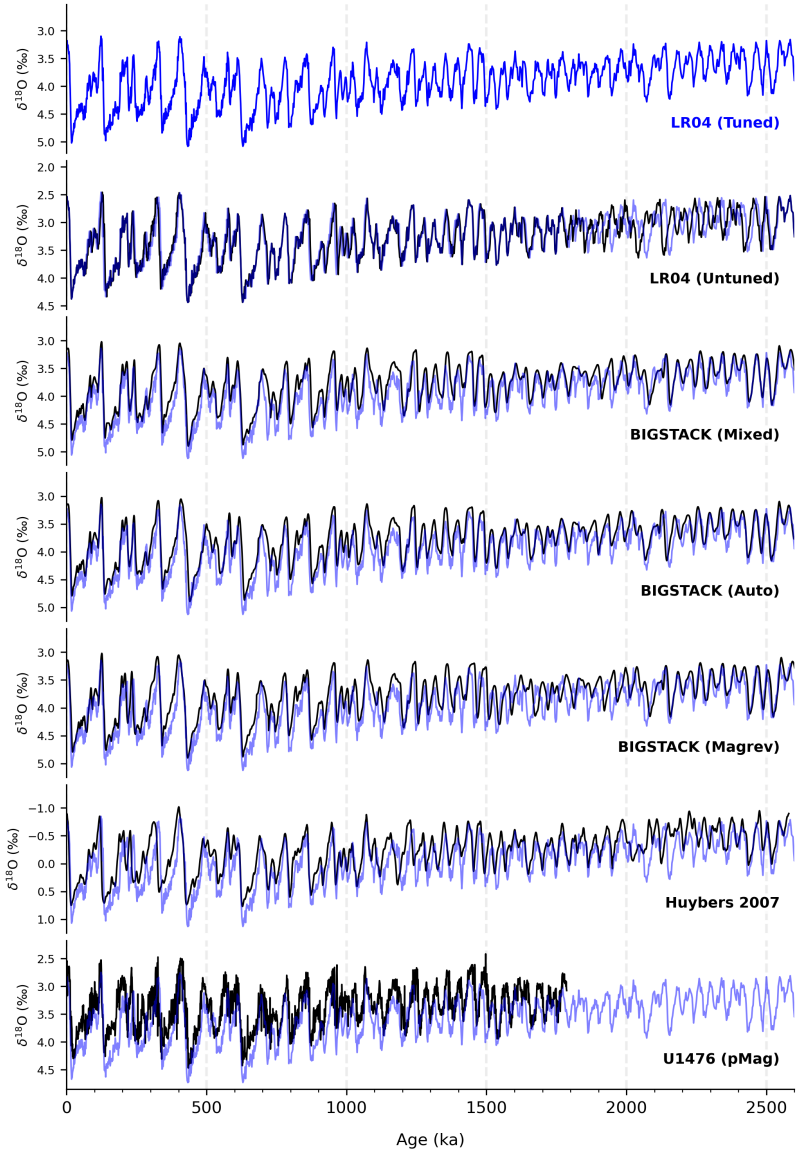

Figure S1: **Benthic δ^{18}O stacks and an individual record analyzed in this study.** (a) The LR04 tuned stack (*6*). In the subsequent panels, the LR04 stack is shown as a blue background reference, vertically shifted to match the mean δ^{18}O value of each target record (black). (b) The tuning-free version of the LR04 stack from Lisiecki (2010) (*34*). (c) The $\text{BIGSTACK}_{\text{mixed}}$ record using speleothem-based age constraints for 0–654 ka and ice-sheet model tuning for earlier intervals (*35*). (d) The $\text{BIGSTACK}_{\text{auto}}$ record obtained from $\text{BIGSTACK}_{\text{magrev}}$ (below) by applying the eTimeOpt algorithm (*36,62*) to minimally tune the pervasive 41-kyr obliquity signal. (e) The $\text{BIGSTACK}_{\text{magrev}}$ record constrained by paleomagnetic events over the last 2.606 Ma to minimize orbital circularity. (f) The depth-derived stack of Huybers (2007) (*37*). (g) The single-site benthic δ^{18}O record from IODP Site U1476, anchored to an independent paleomagnetic age model (U1476pMag) (*25*). This record spans only the last 1786.542 kyr.

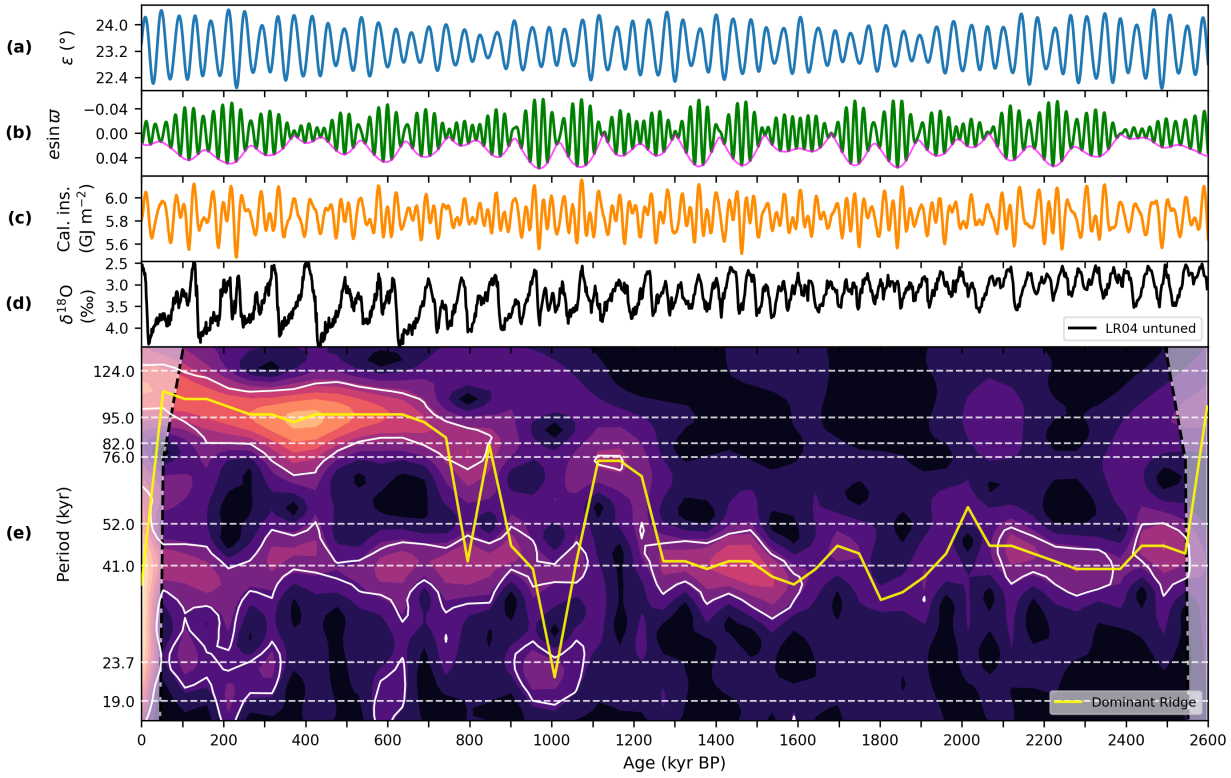

Figure S2: **Time-series and wavelet analyses of the LR04 benthic δ^{18}O stack record free from orbital tuning (*34*), aligned with astronomical forcing (*10*) over the last 2.6 Myr.** (a) Obliquity (ε). (b) Climatic precession ($e \sin \varpi$, green) shown with its eccentricity envelope (e, magenta). (c) Caloric summer half-year insolation at 65°N (*11, 12*). (d) LR04 benthic δ^{18}O stack record without orbital tuning. (*34*) (e) Wavelet power scalogram of the δ^{18}O record. The yellow line indicates the ridge of maximum wavelet power. Areas enclosed by white dashed lines indicate power significant at the 95% confidence level against an AR(1) benchmark. Horizontal dashed lines denote major astronomical periodicities, including the 76-kyr and 52-kyr scales discussed in this study.

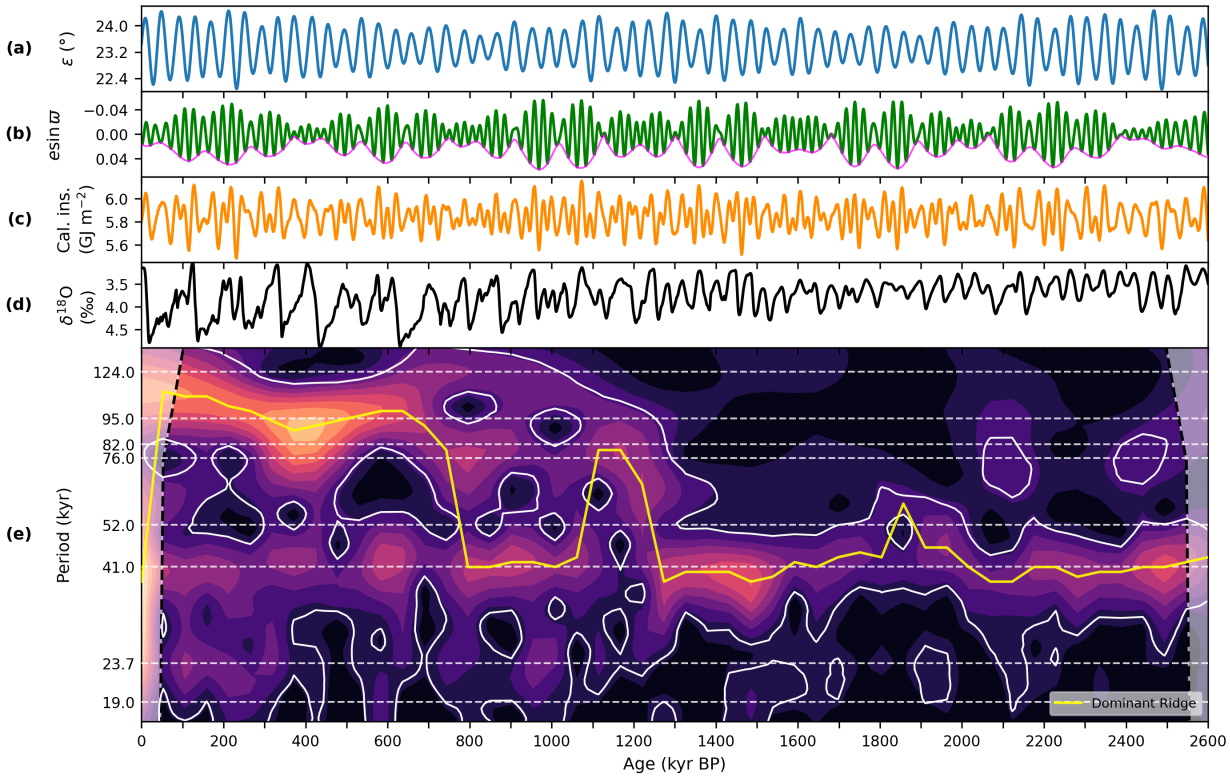

Figure S3: **Time-series and wavelet analyses of the benthic δ^{18}O stack record of BIGSTACK$_{\text{mixed}}$ (*35*), aligned with astronomical forcing (*10*) over the last 2.6 Myr.** (a) Obliquity (ε). (b) Climatic precession ($e \sin \varpi$, green) shown with its eccentricity envelope (e, magenta). (c) Caloric summer half-year insolation at 65°N (*11, 12*). (d) The benthic δ^{18}O stack record of Huybers (2007) (*37*). (e) Wavelet power scalogram of the δ^{18}O record. The yellow line indicates the ridge of maximum wavelet power. Areas enclosed by white dashed lines indicate power significant at the 95% confidence level against an AR(1) benchmark. Horizontal dashed lines denote major astronomical periodicities, including the 76-kyr and 52-kyr scales discussed in this study.

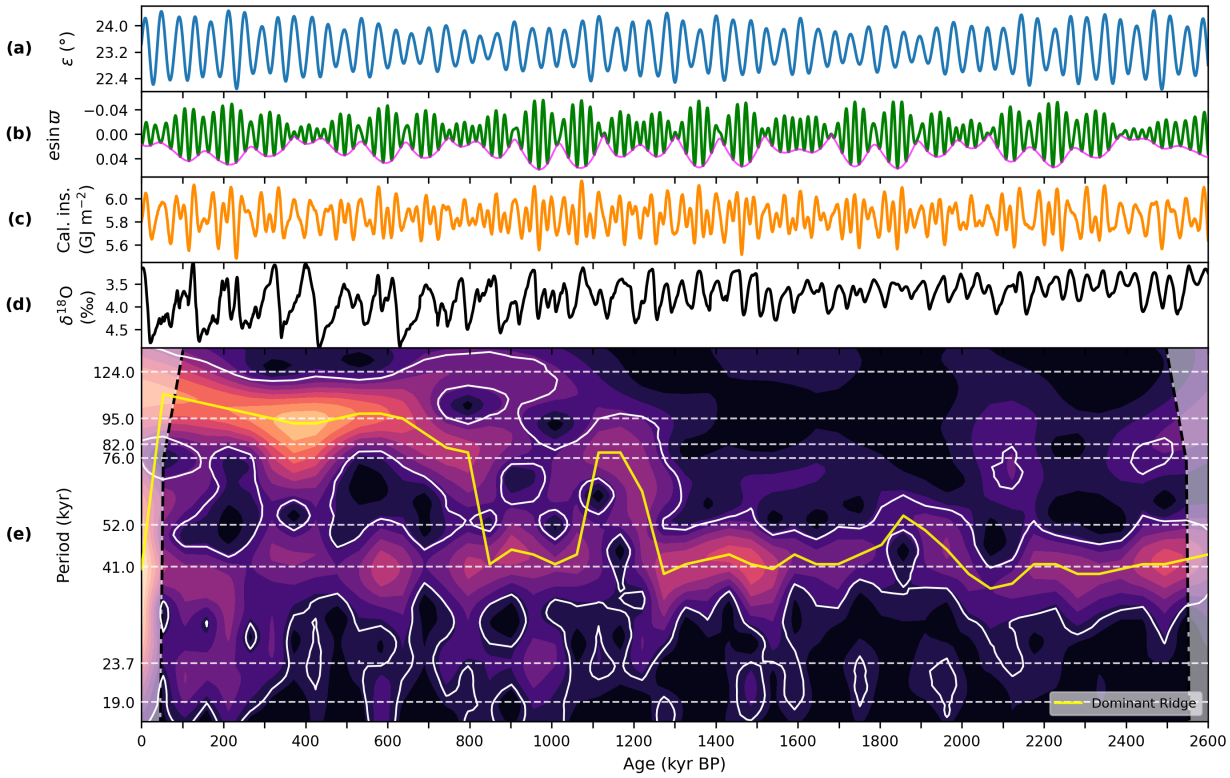

Figure S4: **Time-series and wavelet analyses of the benthic δ^{18}O stack record of BIGSTACK$_{\text{magrev}}$ (*35*), aligned with astronomical forcing (*10*) over the last 2.6 Myr.** (a) Obliquity (ε). (b) Climatic precession ($e \sin \varpi$, green) shown with its eccentricity envelope (e, magenta). (c) Caloric summer half-year insolation at 65°N (*11, 12*). (d) The benthic δ^{18}O stack record of Huybers (2007) (*37*). (e) Wavelet power scalogram of the δ^{18}O record. The yellow line indicates the ridge of maximum wavelet power. Areas enclosed by white dashed lines indicate power significant at the 95% confidence level against an AR(1) benchmark. Horizontal dashed lines denote major astronomical periodicities, including the 76-kyr and 52-kyr scales discussed in this study.

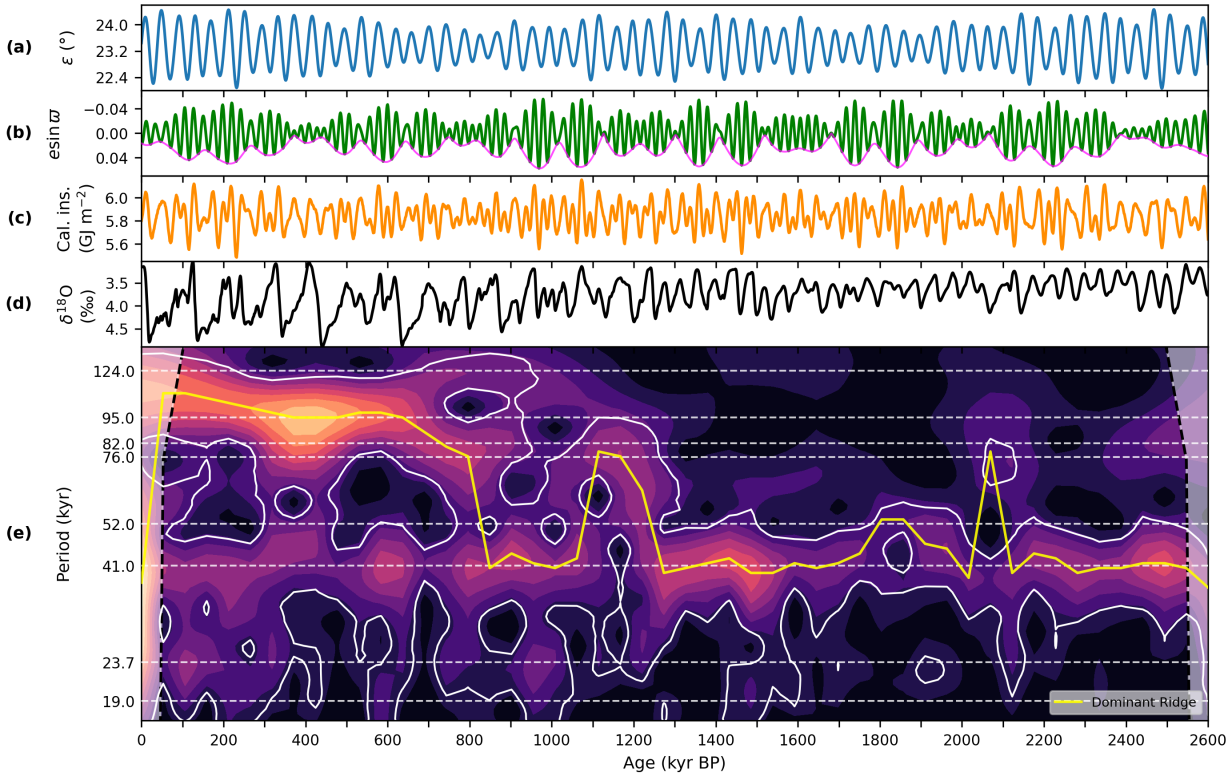

Figure S5: **Time-series and wavelet analyses of the benthic δ^{18}O stack record of BIGSTACK$_{\text{auto}}$ (*35*), aligned with astronomical forcing (*10*) over the last 2.6 Myr.** (a) Obliquity (ε). (b) Climatic precession ($e \sin \varpi$, green) shown with its eccentricity envelope (e, magenta). (c) Caloric summer half-year insolation at 65°N (*11, 12*). (d) The benthic δ^{18}O stack record of Huybers (2007) (*37*). (e) Wavelet power scalogram of the δ^{18}O record. The yellow line indicates the ridge of maximum wavelet power. Areas enclosed by white dashed lines indicate power significant at the 95% confidence level against an AR(1) benchmark. Horizontal dashed lines denote major astronomical periodicities, including the 76-kyr and 52-kyr scales discussed in this study.

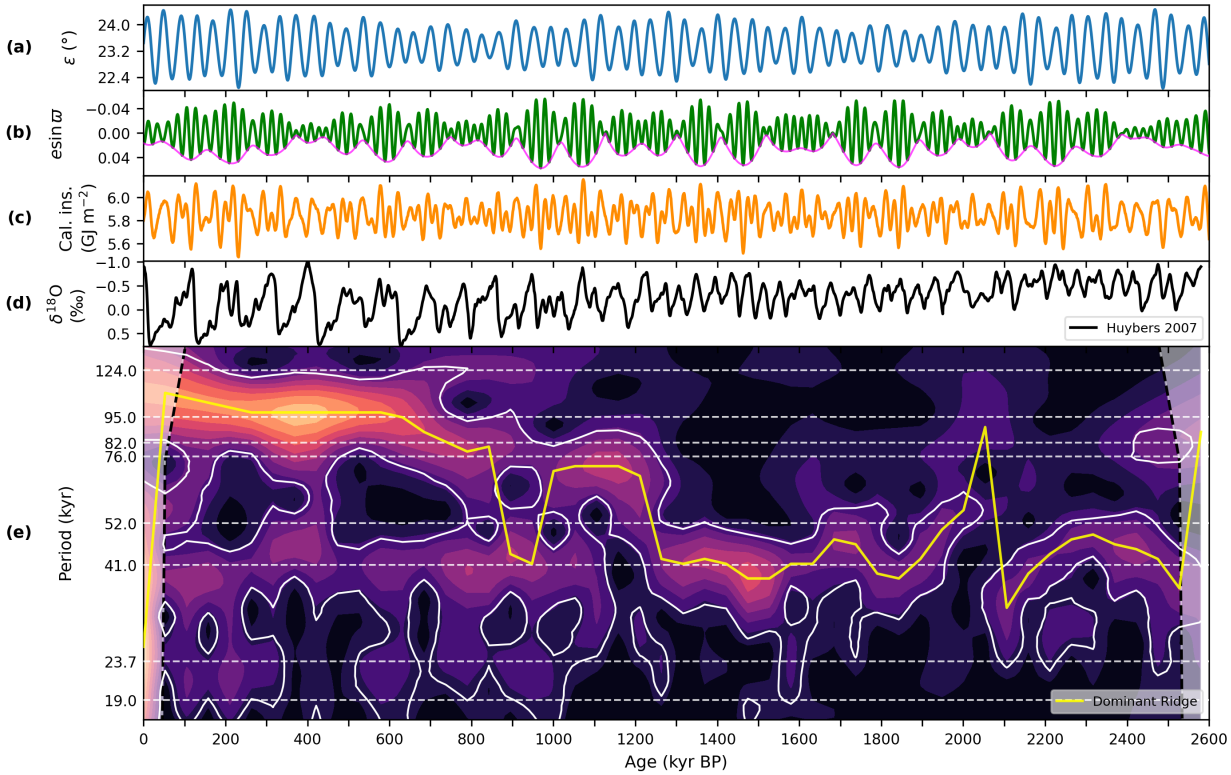

Figure S6: **Time-series and wavelet analyses of the benthic δ^{18}O stack record of Huybers (2007) (*37*), aligned with astronomical forcing (*10*) over the last 2.6 Myr.** (a) Obliquity (ε). (b) Climatic precession ($e \sin \varpi$, green) shown with its eccentricity envelope (e, magenta). (c) Caloric summer half-year insolation at 65°N (*11, 12*). (d) The benthic δ^{18}O stack record of Huybers (2007) (*37*). (e) Wavelet power scalogram of the δ^{18}O record. The yellow line indicates the ridge of maximum wavelet power. Areas enclosed by white dashed lines indicate power significant at the 95% confidence level against an AR(1) benchmark. Horizontal dashed lines denote major astronomical periodicities, including the 76-kyr and 52-kyr scales discussed in this study.

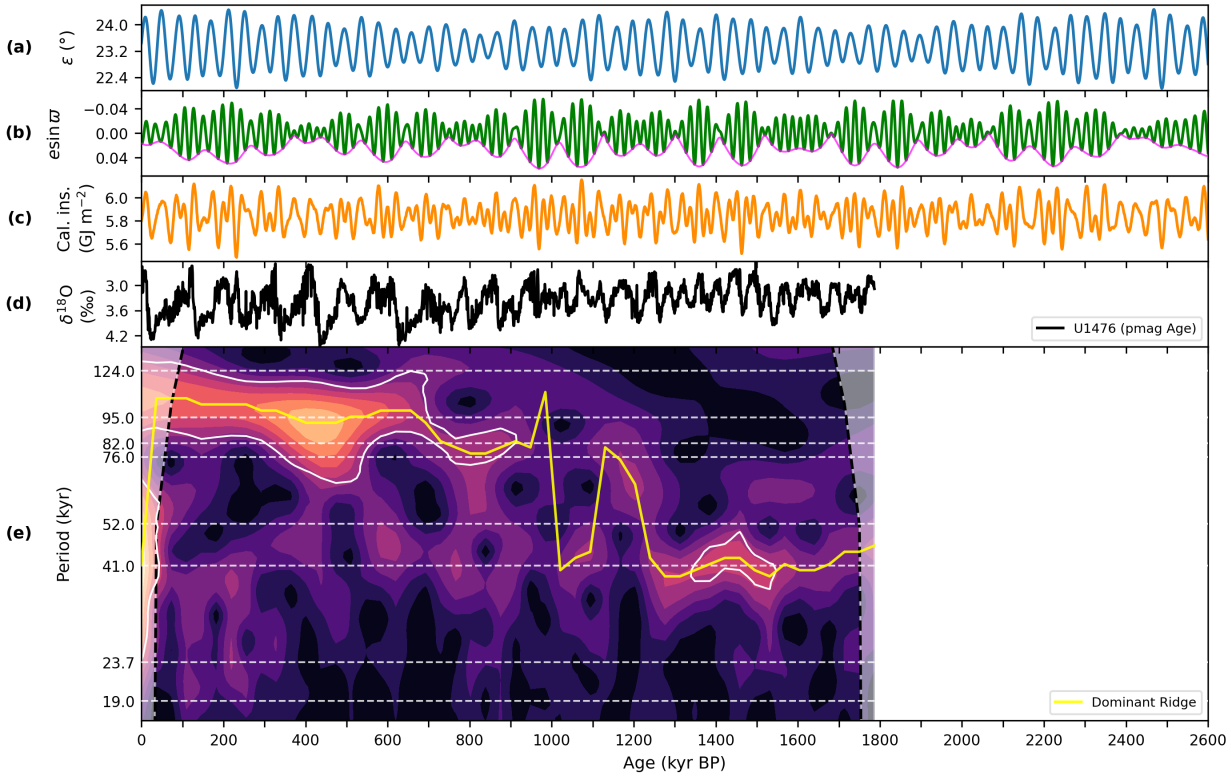

Figure S7: **Time-series and wavelet analyses of the benthic δ^{18}O record from U1476pMag (*25*), aligned with astronomical forcing (*10*) over the last 2.6 Myr.** (a) Obliquity (ε). (b) Climatic precession ($e \sin \varpi$, green) shown with its eccentricity envelope (e, magenta). (c) Caloric summer half-year insolation at 65°N (*11, 12*). (d) The benthic δ^{18}O record from U1476pMag (*25*). (e) Wavelet power scalogram of the δ^{18}O record. The yellow line indicates the ridge of maximum wavelet power. Areas enclosed by white dashed lines indicate power significant at the 95% confidence level against an AR(1) benchmark. Horizontal dashed lines denote major astronomical periodicities, including the 76-kyr and 52-kyr scales discussed in this study.

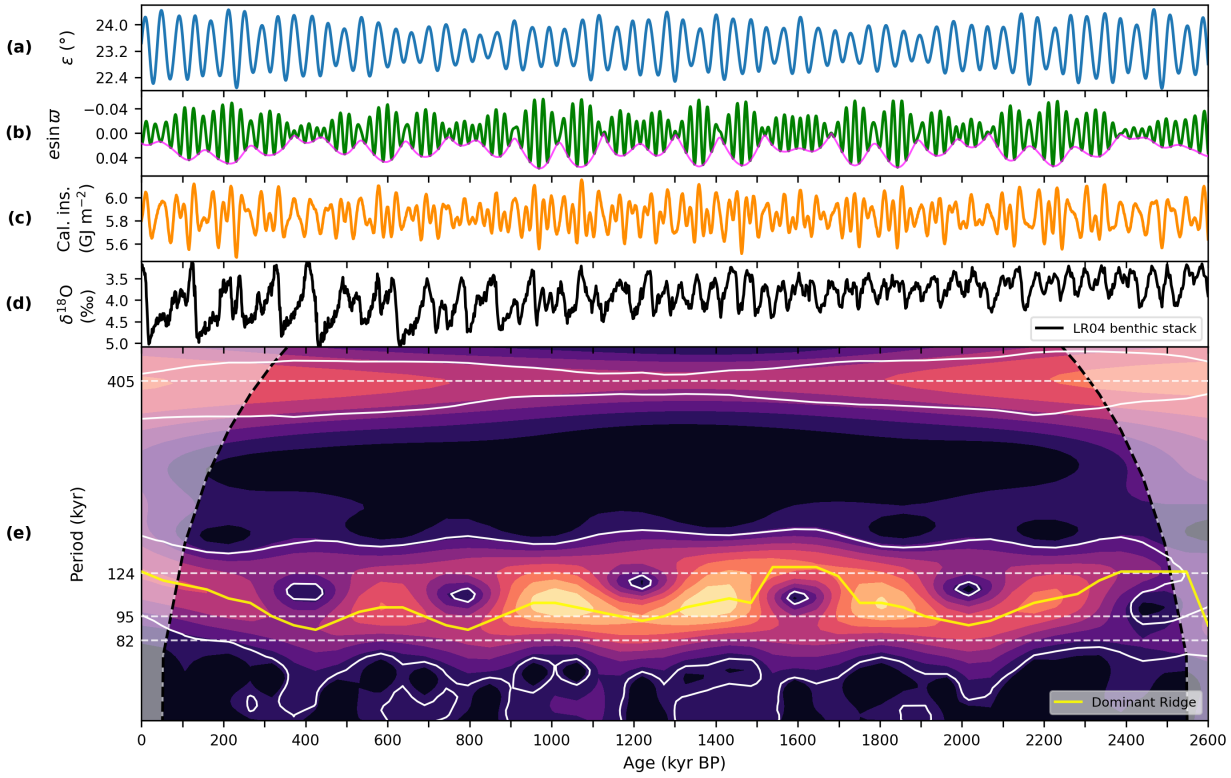

Figure S8: **Time-series and wavelet analyses of eccentricity, aligned with other astronomical elements (*10*) and the LR04 benthic δ^{18}O stack record over the last 2.6 Myr.** (a) Obliquity (ε). (b) Climatic precession ($e \sin \varpi$, green) shown with its eccentricity envelope (e, magenta). (c) Caloric summer half-year insolation at 65°N (*11, 12*). (d) LR04 benthic δ^{18}O stack record without orbital tuning. (*34*) (e) Wavelet power scalogram of eccentricity. The yellow line indicates the ridge of maximum wavelet power obtained by omitting the 405-kyr band. Areas enclosed by white dashed lines indicate power significant at the 95% confidence level against an AR(1) benchmark. Horizontal dashed lines denote major astronomical periodicities of eccentricity.

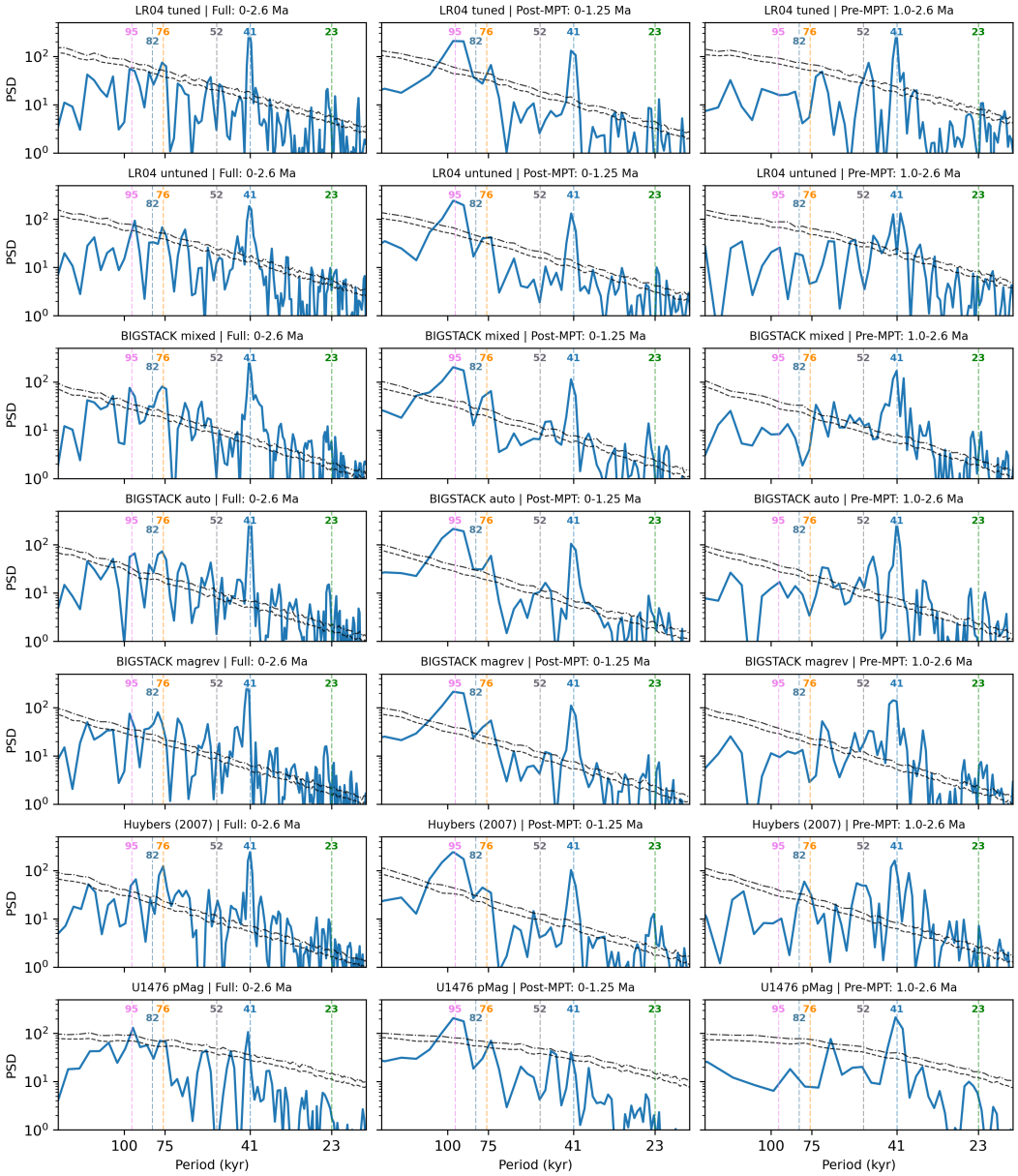

Figure S9: **Comparison of conventional periodograms across multiple benthic δ^{18}O records in Supplementary Information Fig. 1.** Each column represents a specific time interval: the entire Quaternary (0–2.6 Ma; left), the mid-to-late Pleistocene (0–1.25 Ma; center), and the early Pleistocene (1.0–2.6 Ma; right). Blue lines indicate the PSD of the standardized δ^{18}O records, while dashed and dotted black lines denote the 95% and 90% confidence levels, respectively, against an AR(1) benchmark. Vertical dashed lines highlight key periodicities: the canonical eccentricity (95 kyr), obliquity (41 kyr), and precession (23 kyr) cycles, as well as the sub-harmonics analyzed in this study (82, 76, and 52 kyr). The time series is interpolated at 1-kyr intervals before the analysis and then linearly detrended over the analysis period. All analyses are performed using the `pyleoclim` (version 1.2.0) (*33*).

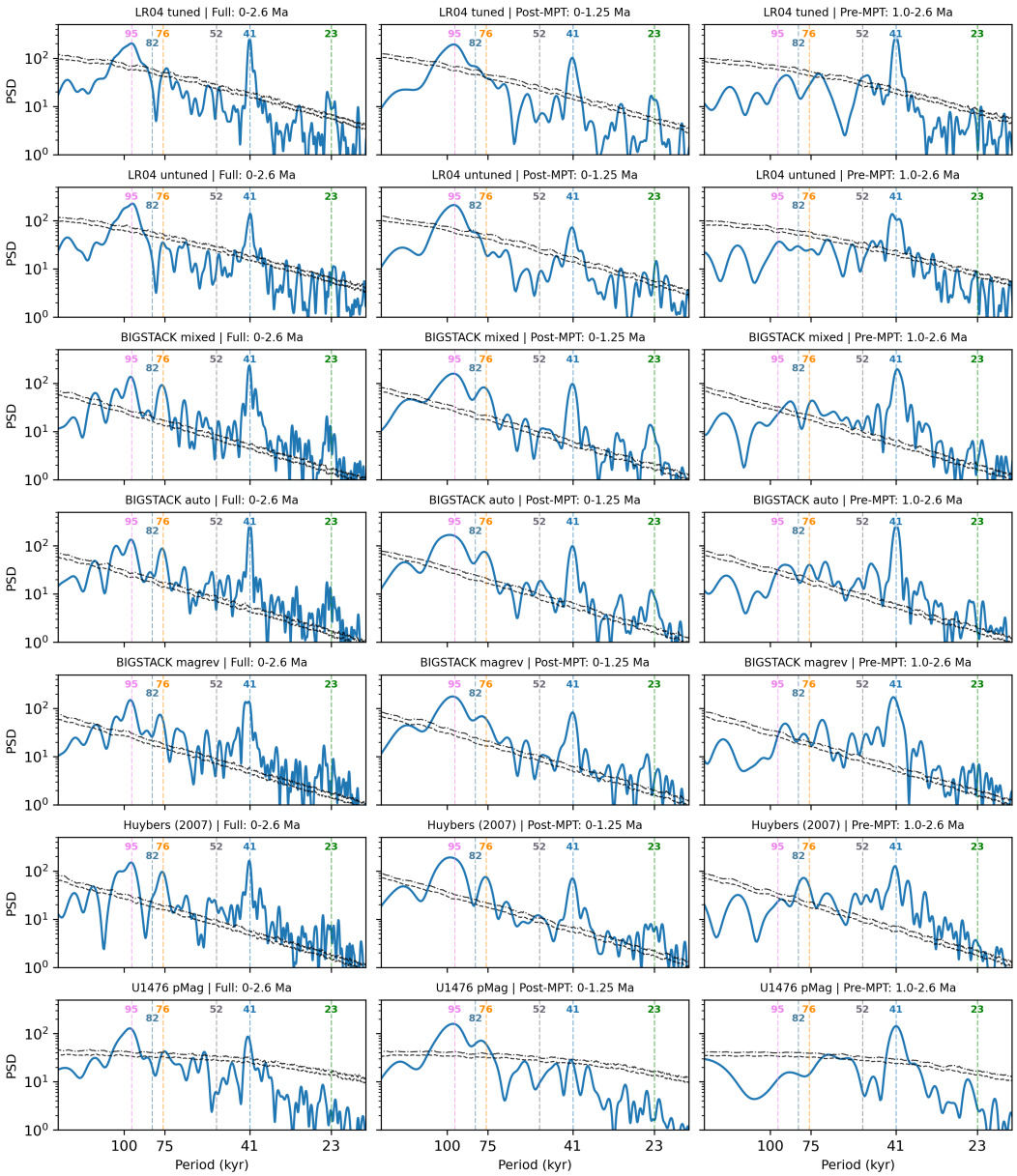

Figure S10: **Comparison of Lomb-Scargle spectra across multiple benthic δ^{18}O records in Supplementary Information Fig. 1.** Each column represents a specific time interval: the entire Quaternary (0–2.6 Ma; left), the mid-to-late Pleistocene (0–1.25 Ma; center), and the early Pleistocene (1.0–2.6 Ma; right). Blue lines indicate the PSD of the standardized δ^{18}O records, while dashed and dotted black lines denote the 95% and 90% confidence levels, respectively, against an AR(1) benchmark. Vertical dashed lines highlight key periodicities: the canonical eccentricity (95 kyr), obliquity (41 kyr), and precession (23 kyr) cycles, as well as the sub-harmonics analyzed in this study (82, 76, and 52 kyr). The series are linearly detrended over the analysis period. All analyses are performed using the `pyleoclim` (version 1.2.0) (*33*).

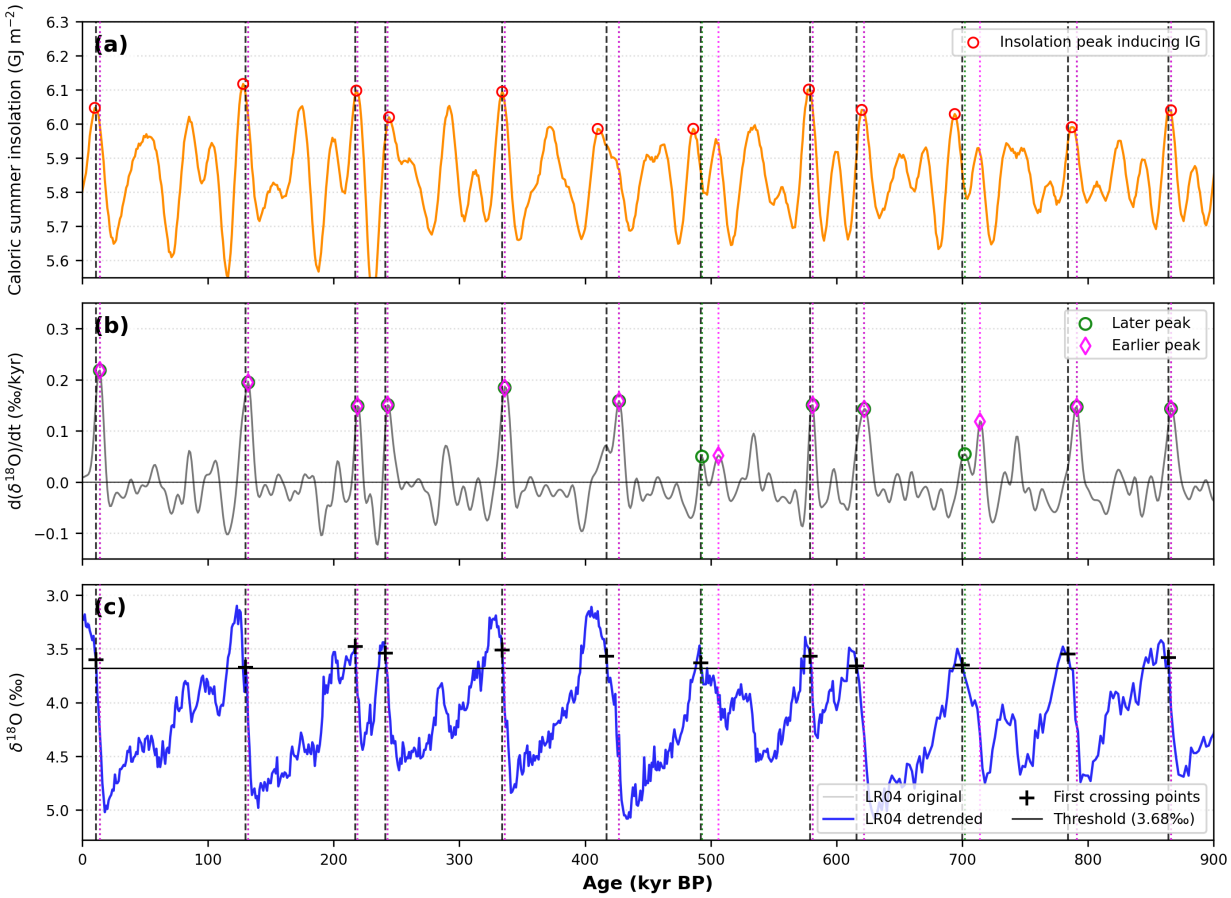

Figure S11: **Detailed deglaciation analysis and timing of interglacial onsets (0–900 ka).** (a) Caloric summer insolation at 65°N (*11, 12*). Red open circles denote the interglacial-inducing insolation peaks (*13*) (see Materials and Methods). (b) The rate of change in benthic δ^{18}O ($d(\delta^{18}\mathrm{O})/dt$) derived from the 10-kyr smoothed LR04 δ^{18}O record. Green circles and magenta diamonds highlight the local maxima in the deglaciation rate, representing later and earlier phases of ice-sheet retreat, respectively. (c) Benthic δ^{18}O records from the LR04 stack. The original record (light gray) is shown alongside the detrended series (*13*) (blue line) used for threshold analysis (see Materials and Methods). Black crosses ('+') mark the first crossing points where the detrended δ^{18}O values exceed the 3.68‰ threshold, defining the onset of interglacial conditions. Vertical dashed lines (black) and dotted lines (green and magenta) indicate the timings of threshold crossings and peak deglaciation rates, respectively, highlighting the phase relationship between each insolation peak and climate response.

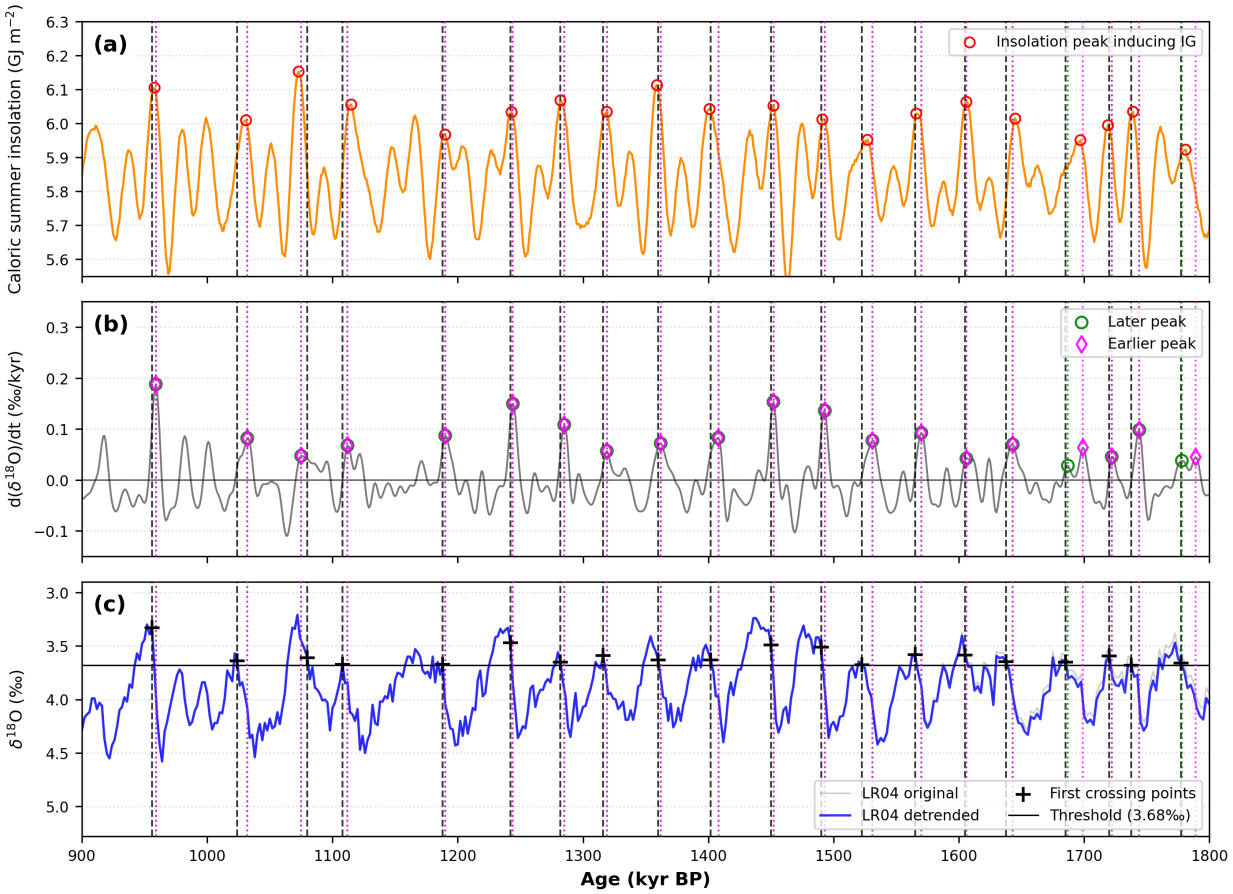

Figure S12: **Detailed deglaciation analysis and timing of interglacial onsets (900–1800 ka).** (a) Caloric summer insolation at 65°N (*11, 12*). Red open circles denote the interglacial-inducing insolation peaks (*13*) (see Materials and Methods). (b) The rate of change in benthic δ^{18}O ($d(\delta^{18}\mathrm{O})/dt$) derived from the 10-kyr smoothed LR04 δ^{18}O record. Green circles and magenta diamonds highlight the local maxima in the deglaciation rate, representing later and earlier phases of ice-sheet retreat, respectively. (c) Benthic δ^{18}O records from the LR04 stack. The original record (light gray) is shown alongside the detrended series (*13*) (blue line) used for threshold analysis (see Materials and Methods). Black crosses ('+') mark the first crossing points where the detrended δ^{18}O values exceed the 3.68‰ threshold, defining the onset of interglacial conditions. Vertical dashed lines (black) and dotted lines (green and magenta) indicate the timings of threshold crossings and peak deglaciation rates, respectively, highlighting the phase relationship between each insolation peak and climate response.

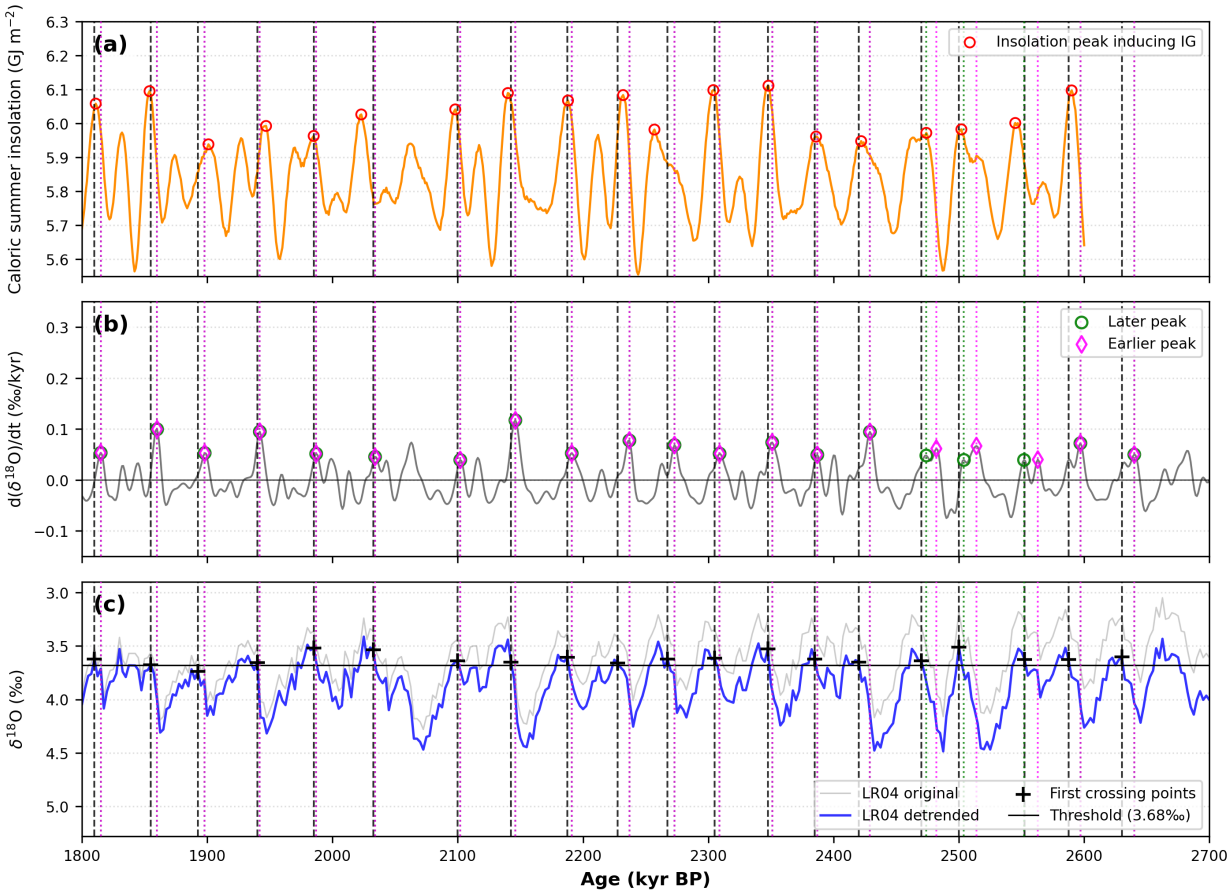

Figure S13: **Detailed deglaciation analysis and timing of interglacial onsets (1800–2700 ka).** (a) Caloric summer insolation at 65°N (*11, 12*). Red open circles denote the interglacial-inducing insolation peaks (*13*) (see Materials and Methods). (b) The rate of change in benthic δ^{18}O ($d(\delta^{18}\mathrm{O})/dt$) derived from the 10-kyr smoothed LR04 δ^{18}O record. Green circles and magenta diamonds highlight the local maxima in the deglaciation rate, representing later and earlier phases of ice-sheet retreat, respectively. (c) Benthic δ^{18}O records from the LR04 stack. The original record (light gray) is shown alongside the detrended series (*13*) (blue line) used for threshold analysis (see Materials and Methods). Black crosses ('+') mark the first crossing points where the detrended δ^{18}O values exceed the 3.68‰ threshold, defining the onset of interglacial conditions. Vertical dashed lines (black) and dotted lines (green and magenta) indicate the timings of threshold crossings and peak deglaciation rates, respectively, highlighting the phase relationship between each insolation peak and climate response.

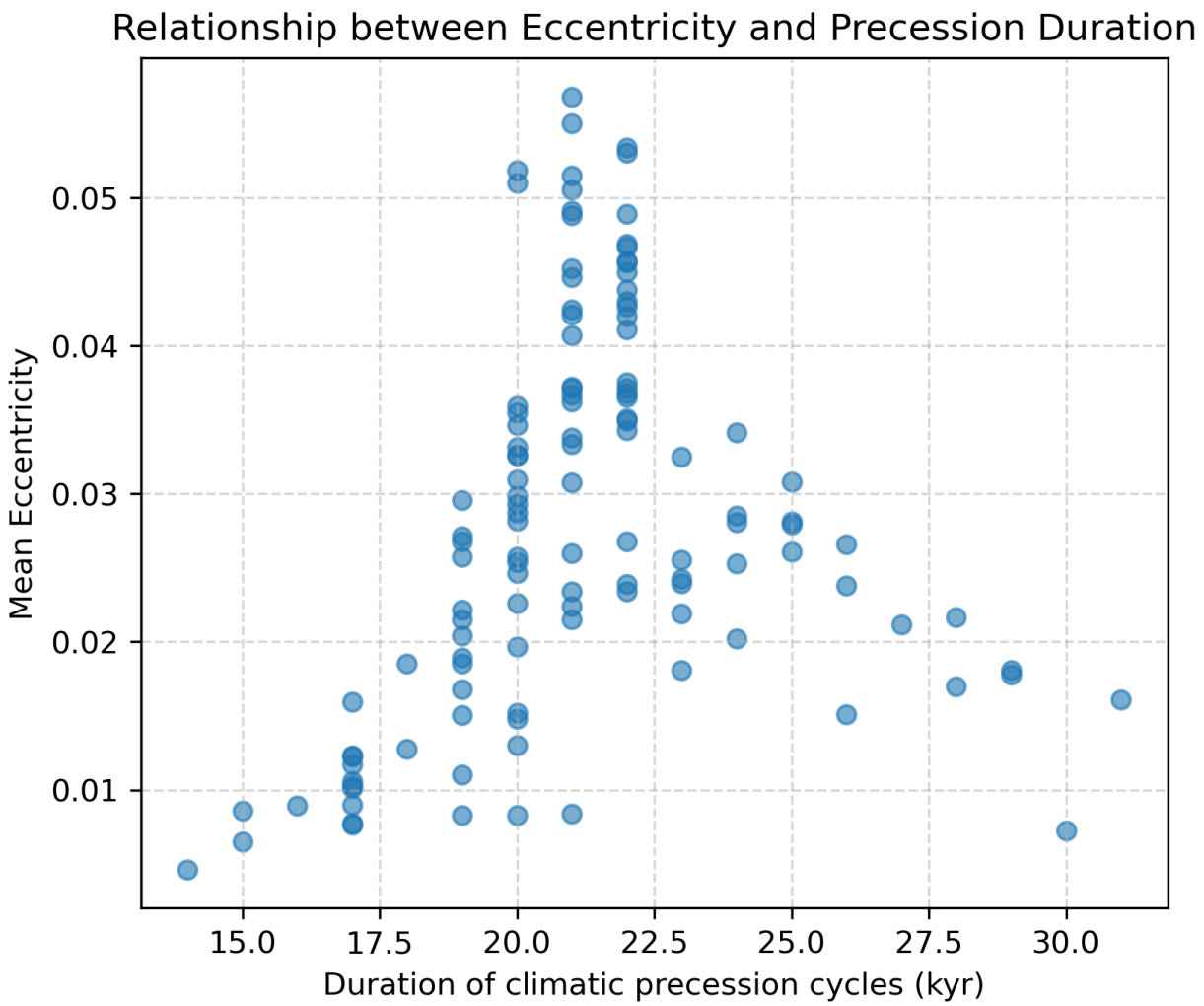

Figure S14: **Relationship between eccentricity and the duration of climatic precession cycles.** The duration of climatic precession cycle is calculated from the spacing between successive precession minima. The local mean of eccentricity is calculated over successive precession minima.

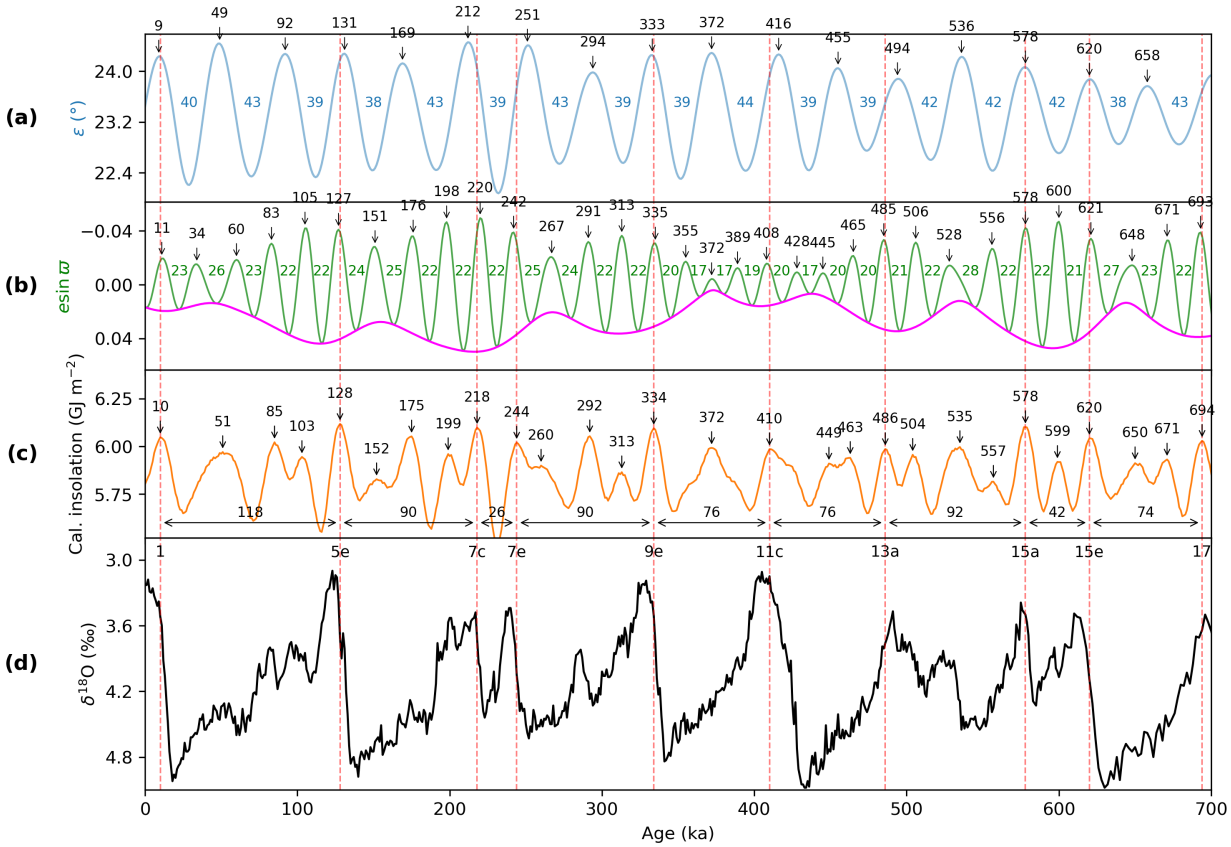

Figure S15: **Orbital forcing and glacial-interglacial cycles over the last 700 kyr.** (a) Obliquity (ε) with peak ages (ka) indicated by arrows. Peak-to-peak spacings are shown in blue between consecutive peaks. (b) Climatic precession ($e \sin \varpi$, green) and eccentricity (e, magenta). Note that the $e \sin \varpi$ axis is inverted to align with insolation peaks. Peak-to-peak spacings are shown in green between consecutive minima. (c) Caloric summer half-year insolation at 65°N (*11, 12*). Horizontal double-headed arrows indicate the interglacial spacings (T_{ins}), where values correspond to the spacings between interglacial-inducing insolation maxima. (d) LR04 δ^{18}O stack (*6*). Numbers at the top denote Marine Isotope Stages (MIS). Vertical red dashed lines across all panels mark the timing of insolation peaks that induced interglacials (*13*). The orbital solutions are from Laskar et al. (2004) (*10*).

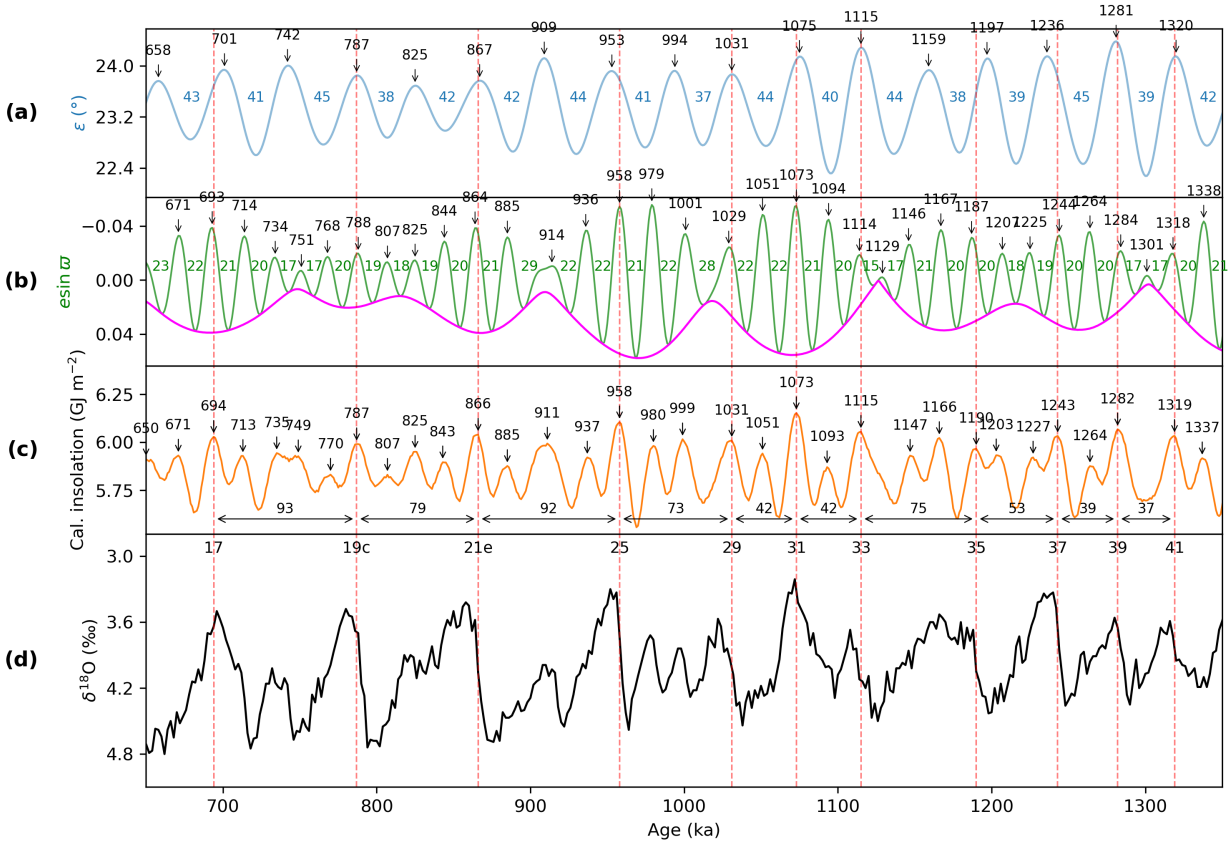

Figure S16: **Orbital forcing and glacial-interglacial cycles from 650 to 1350 ka.** (a) Obliquity (ε) with peak ages (ka) indicated by arrows. Peak-to-peak spacings are shown in blue between consecutive peaks. (b) Climatic precession ($e \sin \varpi$, green) and eccentricity (e, magenta). Note that the $e \sin \varpi$ axis is inverted to align with insolation peaks. Peak-to-peak spacings are shown in green between consecutive minima. (c) Caloric summer half-year insolation at 65°N (*11, 12*). Horizontal double-headed arrows indicate the interglacial spacings (T_{ins}), where values correspond to the spacings between interglacial-inducing insolation maxima. (d) LR04 δ^{18}O stack (*6*). Numbers at the top denote Marine Isotope Stages (MIS). Vertical red dashed lines across all panels mark the timing of insolation peaks that induced interglacials (*13*). The orbital solutions are from Laskar et al. (2004) (*10*).

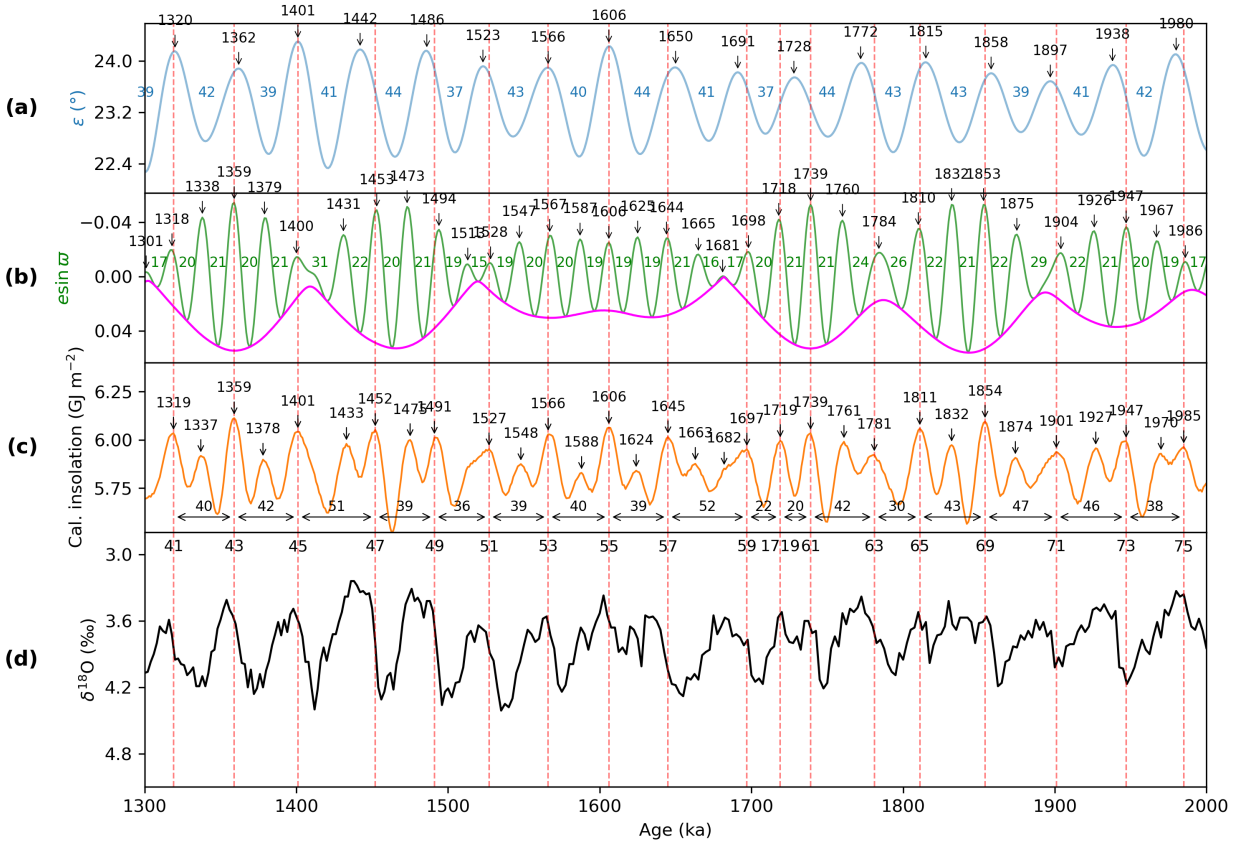

Figure S17: **Orbital forcing and glacial-interglacial cycles from 1300 to 2000 ka.** (a) Obliquity (ε) with peak ages (ka) indicated by arrows. Peak-to-peak spacings are shown in blue between consecutive peaks. (b) Climatic precession ($e \sin \varpi$, green) and eccentricity (e, magenta). Note that the $e \sin \varpi$ axis is inverted to align with insolation peaks. Peak-to-peak spacings are shown in green between consecutive minima. (c) Caloric summer half-year insolation at 65°N (*11, 12*). Horizontal double-headed arrows indicate the interglacial spacings (T_{ins}), where values correspond to the spacings between interglacial-inducing insolation maxima. (d) LR04 δ^{18}O stack (*6*). Numbers at the top denote Marine Isotope Stages (MIS). Vertical red dashed lines across all panels mark the timing of insolation peaks that induced interglacials (*13*). The orbital solutions are from Laskar et al. (2004) (*10*).

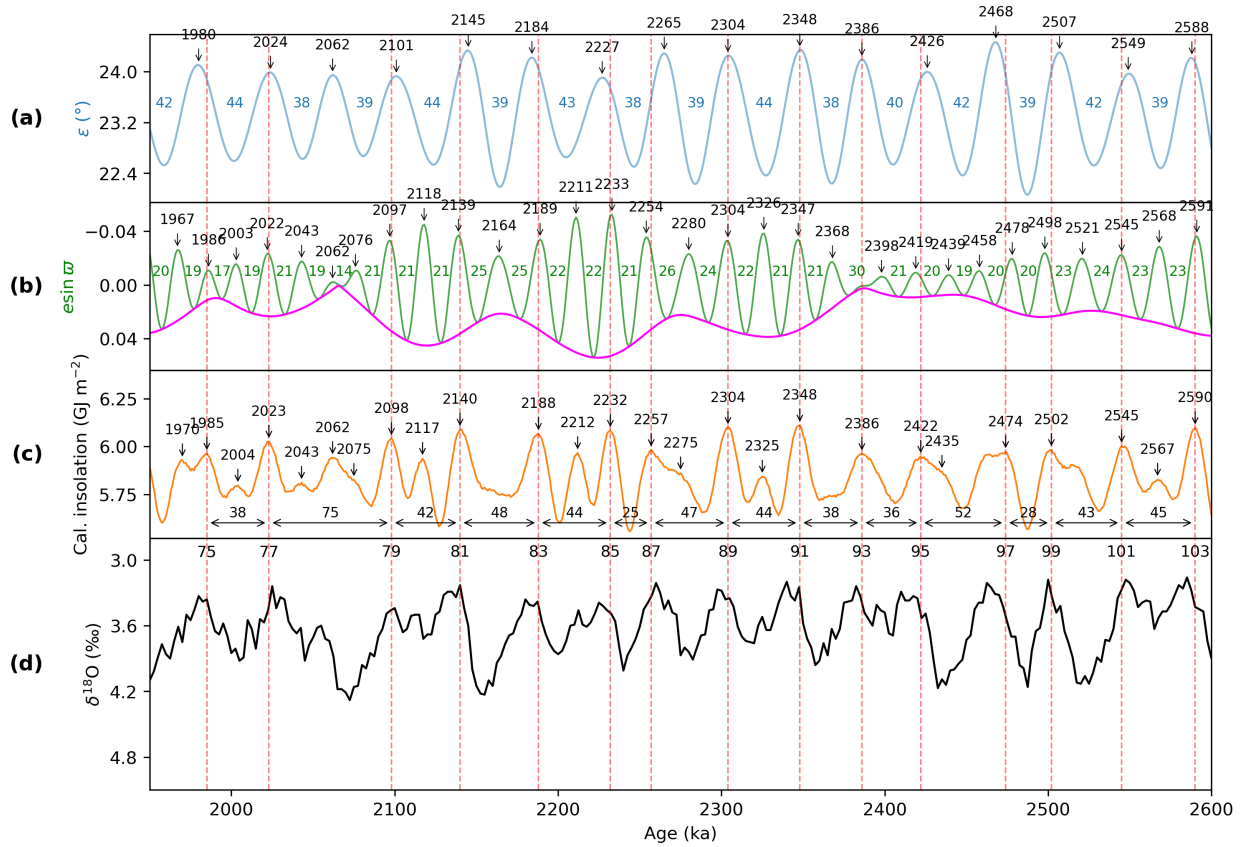

Figure S18: **Orbital forcing and glacial-interglacial cycles from 1950 to 2600 ka. (a) Obliquity (ε) with peak ages (ka) indicated by arrows.** Peak-to-peak spacings are shown in blue between consecutive peaks. (b) Climatic precession ($e \sin \varpi$, green) and eccentricity (e, magenta). Note that the $e \sin \varpi$ axis is inverted to align with insolation peaks. Peak-to-peak spacings are shown in green between consecutive minima. (c) Caloric summer half-year insolation at 65°N (*11, 12*). Horizontal double-headed arrows indicate the interglacial spacings (T_{ins}), where values correspond to the spacings between interglacial-inducing insolation maxima. (d) LR04 δ^{18}O stack (*6*). Numbers at the top denote Marine Isotope Stages (MIS). Vertical red dashed lines across all panels mark the timing of insolation peaks that induced interglacials (*13*). The orbital solutions are from Laskar et al. (2004) (*10*).

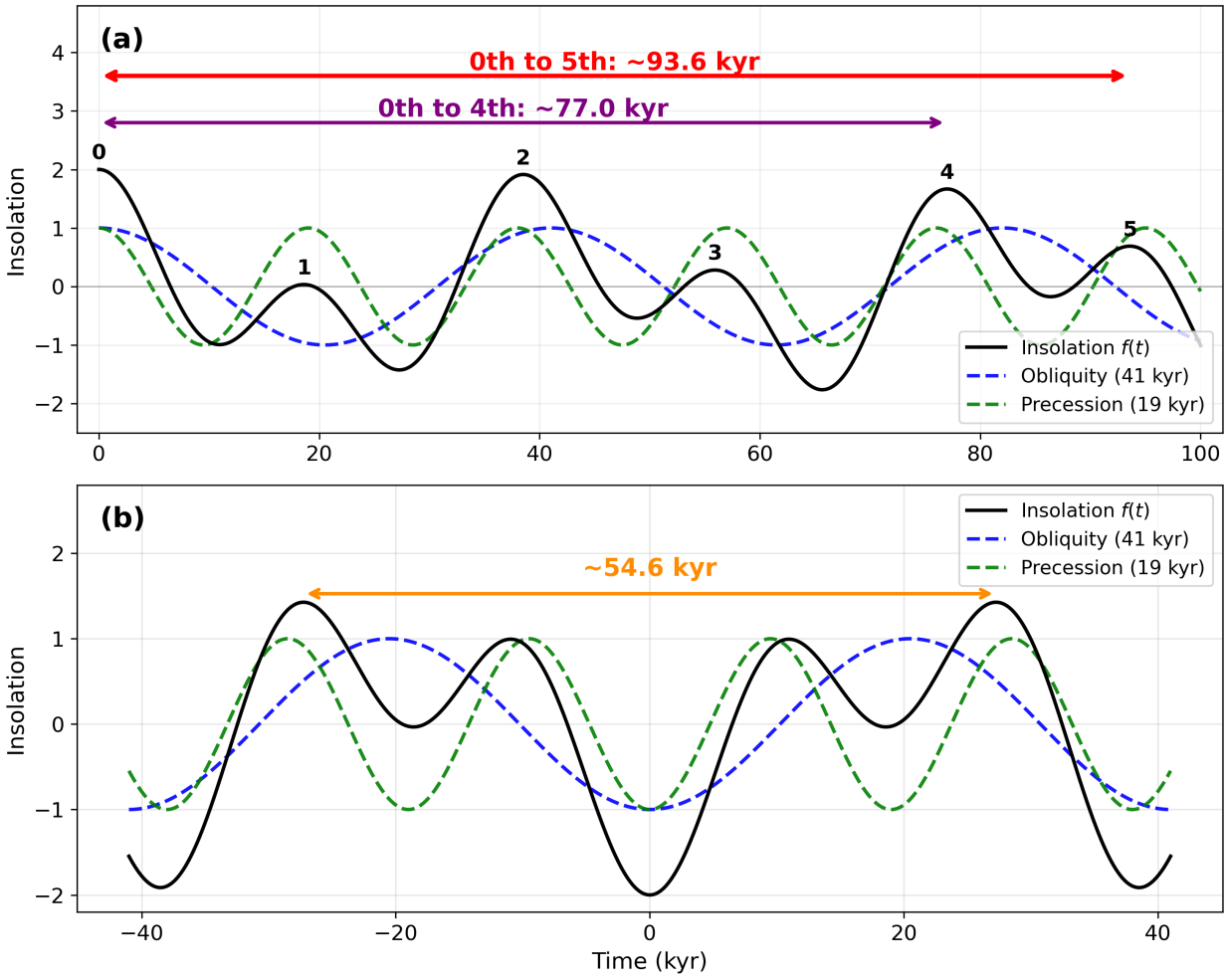

Figure S19: **Schematic representation of an insolation curve approximated by two harmonic components.** The insolation curve is assumed to be represented as the sum of two harmonic components: $\cos(2\pi t/19)$ (climatic precession) and $\cos(2\pi t/41)$ (obliquity). (a) The insolation curve is given by $f(t) = \cos(2\pi t/19) + \cos(2\pi t/41)$. (b) The insolation curve is given by $f(t) = -\cos(2\pi t/19) - \cos(2\pi t/41)$.

Supporting Information Table S1 for "Beyond the 100-kyr and 41-kyr dichotomy: ~76- and ~52-kyr signals and forbidden periodicities in Quaternary glacial cycles" by Takahito Mitsui

Creater: Takahito Mitsui (Juntendo University). (email: takahito321ATgmail.com)

Date: 2 April 2026

Description:

This sheet shows the calculation of the insolation-based inter-deglaciation intervals (T_ins) by using the approximation formulae described in Supporting Information document.

The calotic summer half-year insolation at 65N is chosen as the insolation metric following Tzedakis et al. Nature (2017). It is calculated based on the orbital solution of Laskar et al. A&A (2004) using R-package 'Palinsol' created by Michel Crucifix.

The insolation-based inter-deglaciation interval (T_ins) between two interglacials (called "start" and "end" below) is approximately given by the spacing between two insolation peaks that induce interglacials.

Marine Isotope Stage (MIS) of interglacial "end"	Marine Isotope Stage (MIS) of interglacial "start"	Insolation peak "end" (ka)	Insolation peak "start" (ka)	Actual inter-deglaciation interval (T_ins) (kyr)	Precession (esin) peak "end" (ka)	Precession (esin) peak "start" (ka)	Number of precession cycles	Local-mean precession period T_p (kyr)	Obliquity peak "end" (ka)	Obliquity peak "start" (ka)	Number of obliquity cycles	Local-mean obliquity period (kyr)	Formula type	Predicted Inter-deglaciation interval (T_ins) (kyr)	Difference = predicted T_ins - actual T_ins (kyr)	T_later (kyr)	T_earlier (kyr)
1	5e	10	128	118	11	127	5	23.2	9	131	3	40.66666667	5a	117.4095046	-0.590495389	118	118
5e	7c	128	218	90	127	220	4	23.25	131	212	2	40.5	4a	90.75253717	0.752537167	87	87
7c	7e	218	244	26	220	242	1	22	212	251	1	39	1b	25.63885892	-0.36114108	24	24
7e	9e	244	334	90	242	335	4	23.25	251	333	2	41	4a	90.83565547	0.835655466	93	93
9e	11c	334	410	76	335	408	4	18.25	333	416	2	41.5	4a	74.26141357	-1.738586426	91	91
11c	13a	410	486	76	408	485	4	19.25	416	494	2	39	pp	77	1	66	79
13a	15a	486	578	92	485	578	4	23.25	494	578	2	42	4a	91.13043353	-0.86956647	88	75
15a	15e	578	620	42	578	621	2	21.5	578	620	1	42	2a	42.7926566	0.792656604	41	41
15e	17	620	694	74	621	693	3	24	620	701	2	40.5	3a	74.10102939	0.101029386	80	92
17	19c	694	787	93	693	788	5	19	701	787	2	43	5a	93.76811957	0.768119566	89	77
19c	21e	787	866	79	788	864	4	19	787	867	2	40	4b	76.73089134	-2.26910866	75	75
21e	25	866	958	92	864	958	4	23.5	867	953	2	43	4a	92.31555016	0.315550159	93	93
25	29	958	1031	73	958	1029	3	23.66666667	953	1031	2	39	3a	72.7835095	-0.216490502	73	73
29	31	1031	1073	42	1029	1073	2	22	1031	1075	1	44	2a	44	2	43	43
31	33	1073	1115	42	1073	1114	2	20.5	1075	1115	1	40	2a	40.79230366	-1.207696343	37	37
33	35	1115	1190	75	1114	1187	4	18.25	1115	1197	2	41	4a	74.22310319	-0.776896814	78	78
35	37	1190	1243	53	1187	1244	3	19	1197	1236	1	39	3b	54.1564265	1.156426499	54	54
37	39	1243	1282	39	1244	1284	2	20	1236	1281	1	45	pp	40	1	41	41
39	41	1282	1319	37	1284	1318	2	17	1281	1320	1	39	2b	34.78698727	-2.213012733	34	34
41	43	1319	1359	40	1318	1359	2	20.5	1320	1362	1	42	pp	41	1	43	43
43	45	1359	1401	42	1359	1400	2	20.5	1362	1401	1	39	pp	41	-1	46	46
45	47	1401	1452	51	1400	1453	2	26.5	1401	1442	1	41	2a	50.04423465	-0.955765345	44	44
47	49	1452	1491	39	1453	1494	2	20.5	1442	1486	1	44	2c	39.73163334	0.731633338	41	41
49	51	1491	1527	36	1494	1528	2	17	1486	1523	1	37	pp	34	-2	38	38
51	53	1527	1566	39	1528	1567	2	19.5	1523	1566	1	43	2a	39.6628726	0.662872597	39	39
53	55	1566	1606	40	1567	1606	2	19.5	1566	1606	1	40	2a	39.19168569	-0.808314308	36	36
55	57	1606	1645	39	1606	1644	2	19	1606	1650	1	44	2a	38.87946221	-0.12053779	37	37
57	59	1645	1697	52	1644	1698	3	18	1650	1691	1	41	3b	52.08886632	0.088866322	44	56
59	1719	1697	1719	22	1698	1718	1	20	1691	1728	1	37	1c	21.5508926	-0.449107399	35	23
1719	61	1719	1739	20	1718	1739	1	21	1728	1728	0	#DIV/0!	pp	21	1	22	22
61	63	1739	1781	42	1739	1784	2	22.5	1728	1772	1	44	2c	43.11739279	1.117392788	34	45
63	65	1781	1811	30	1784	1810	1	26	1772	1815	1	43	1b	30.23605565	0.236055654	37	2
65	69	1811	1854	43	1810	1853	2	21.5	1815	1858	1	43	pp	43	0	45	45
69	71	1854	1901	47	1853	1904	2	25.5	1858	1897	1	39	2b	47.48572001	0.485720005	38	38
71	73	1901	1947	46	1904	1947	2	21.5	1897	1938	1	41	2d	44.86553125	-1.134468748	44	44
73	75	1947	1985	38	1947	1986	2	19.5	1938	1980	1	42	2c	37.81281134	-0.187188656	45	45
75	77	1985	2023	38	1986	2022	2	18	1980	2024	1	44	2b	37.11082651	-0.889173493	47	47
77	79	2023	2098	75	2022	2097	4	18.75	2024	2101	2	38.5	4b	75.38269763	0.382697632	68	68
79	81	2098	2140	42	2097	2139	2	21	2101	2145	1	44	pp	42	0	44	44
81	83	2140	2188	48	2139	2189	2	25	2145	2184	1	39	2b	46.86370843	-1.136291572	45	45
83	85	2188	2232	44	2189	2233	2	22	2184	2227	1	43	2b	43.79261153	-0.207388473	46	46
85	87	2232	2257	25	2233	2254	1	21	2227	2265	1	38	1b	24.46929504	-0.53070496	3	36
87	89	2257	2304	47	2254	2304	2	25	2265	2304	1	39	2a	47.27718819	0.277188193	36	36
89	91	2304	2348	44	2304	2347	2	21.5	2304	2348	1	44	2a	43.19246791	-0.807532094	42	42
91	93	2348	2386	38	2347	2398	2	25.5	2348	2386	1	38	O2-(P1+C	38.5	0.5	36	36
93	95	2386	2422	36	2398	2419	1	21	2386	2426	1	40	(O2+P2)/	36.5	0.5	42	42
95	97	2422	2474	52	2419	2478	3	19.66666667	2426	2468	1	42	3b*	51.96142631	-0.038573691	45	53
97	99	2474	2502	28	2478	2498	1	20	2468	2507	1	39	1b*	27.94484616	-0.055153836	30	32
99	101	2502	2545	43	2498	2545	2	23.5	2507	2549	1	42	2c	45.05090417	2.050904171	48	49
101	103	2545	2590	45	2545	2591	2	23	2549	2588	1	39	2b	44.21662793	-0.78337207	45	34

Note: Special rules are emploied for MIS 99-97, 97-95, 95-93, and 93-91, where eccentricity is particularly low. See Supplementary Note.